Correlative light and electron microscopy reveals the fine circuit structure underlying evidence accumulation in larval zebrafish

Authors

Jonathan Boulanger-Weill[1,2,6,8], Florian Kämpf[3,6], Richard L. Schalek[1], Mariela Petkova[1], Sumit Kumar Vohra[4], Jay H. Savaliya[1], Yuelong Wu[1], Gregor F. P. Schuhknecht[1], Heike Naumann[3], Maren Eberle[1], Kim N. Kirchberger[3], Simone Rencken[1], Isaac H. Bianco[5], Daniel Baum[4], Filippo Del Bene[2,7], Florian Engert[1,7], Jeff W. Lichtman[1,7], Armin Bahl[3,7,8]

Affiliations

1: Department of Molecular and Cellular Biology, Faculty of Arts and Sciences, Harvard University, Cambridge, MA 02138, USA

2: Sorbonne Université, CNRS, Inserm, Institut de la Vision, F-75012 Paris, France

3: Centre for the Advanced Study of Collective Behaviour, University of Konstanz, Konstanz, Germany

4: Department of Visual and Data-Centric Computing, Zuse Institute Berlin (ZIB), Berlin, Germany

5: Department of Neuroscience, Physiology & Pharmacology, University College London, London, United Kingdom

6: These authors contributed equally: Jonathan Boulanger-Weill, Florian Kämpf

7: These authors jointly supervised this work: Filippo Del Bene, Florian Engert, Jeff W. Lichtman, Armin Bahl

8: Corresponding authors: boulangerweill@fas.harvard.edu; armin.bahl@uni-konstanz.de

Abstract

Accumulating information is a critical component of most circuit computations in the brain across species, yet its precise implementation at the synaptic level remains poorly understood. Dissecting such neural circuits in vertebrates requires precise knowledge of functional neural properties and the ability to directly correlate neural dynamics with the underlying wiring diagram in the same animal. Here we combine functional calcium imaging with ultrastructural circuit reconstruction, using a visual motion accumulation paradigm in larval zebrafish. Using connectomic analyses of functionally identified cells and computational modeling, we show that bilateral inhibition, disinhibition, and recurrent connectivity are prominent motifs for sensory accumulation within the anterior hindbrain. We also demonstrate that similar insights about the structure-function relationship within this circuit can be obtained through complementary methods involving cell-specific morphological labeling via photo-conversion of functionally identified neuronal response types. We used our unique ground truth datasets to train and test a novel classifier algorithm, allowing us to assign functional labels to neurons from morphological libraries where functional information is lacking. The resulting feature-rich library of neuronal identities and connectomes enabled us to constrain a biophysically realistic network model of the anterior hindbrain that can reproduce observed neuronal dynamics and make testable predictions for future experiments. Our work exemplifies the power of hypothesis-driven electron microscopy paired with functional recordings to gain mechanistic insights into signal processing and provides a framework for dissecting neural computations across vertebrates.

Introduction

In natural environments, behaviorally relevant signals are often noisy, fragmented, or conflicting. To navigate this complexity and make reliable decisions, animals must continuously accumulate sensory information across space and time. This fundamental computation for selecting appropriate actions has been observed in a wide range of species including flies (Groschner *et al.*, 2018), fish (Bahl and Engert, 2020; Dragomir, Štih and Portugues, 2020), rodents (Hanks *et al.*, 2015) and primates (Katz *et al.*, 2016). A classic approach for studying this process is through random dot motion kinematograms, where some flickering dots move coherently while others are randomly redrawn across the visual field. This stimulus has been used alongside single-neuron and population-level recordings to reveal ramping neural responses, with slopes correlated with coherence levels, indicative of sensory accumulation of evidence (Newsome, Britten and Movshon, 1989; Hanks and Summerfield, 2017). Recent findings suggest that this integration is distributed throughout the mammalian brain, involving both cortical and subcortical regions (Brody and Hanks, 2016). However, the detailed architecture—both at the synaptic and whole-brain levels—that transforms noisy sensory input into discrete motor actions in vertebrates remains unclear.

The zebrafish larva (*Danio rerio*) also responds to random dot motion, accumulating visual evidence of self-motion before initiating stabilizing motor commands (Bahl and Engert, 2020; Dragomir, Štih and Portugues, 2020). Its compact brain and genetic amenability make it a powerful model for investigating neural computations using light microscopy, enabling whole-brain functional circuit dissection that is not feasible in larger vertebrates. Previous research has highlighted the anterior hindbrain, where neurons display calcium dynamics indicative of visual evidence accumulation, as a key computational hub for this process (Bahl and Engert, 2020; Dragomir, Štih and Portugues, 2020). Several network predictions have been proposed: hindbrain neurons accumulate pretectal (Pt) sensory input by recurrent connectivity of excitatory neurons, generating persistent activity (Yang *et al.*, 2023). Faster-dynamics neurons in this region were suggested to establish a decision boundary, filtering out low-quality stimuli by inhibiting premature motor activation (Bahl and Engert, 2020). Originating from this area, motor command neurons provide excitatory and inhibitory inputs to distinct pools of reticulospinal neuron subtypes, each tuned to specific movement directions, thereby selecting the appropriate motor output (Orger *et al.*, 2008; Kubo *et al.*, 2014; Naumann *et al.*, 2016).

Volumetric electron microscopy techniques have made it possible to map synaptic connectivity with remarkable resolution in several invertebrate and vertebrate species (Witvliet *et al.*, 2021; Svara *et al.*, 2022; Turner *et al.*, 2022; Schlegel *et al.*, 2024; Shapson-Coe *et al.*, 2024). In *Drosophila*, this connectomic data, when combined with complementary methods such as electrophysiology, optogenetics, and behavioral analysis, can refine models of neural networks (Turner-Evans *et al.*, 2020; Ammer *et al.*, 2023), predict neural dynamics (Lappalainen *et al.*, 2024; Shiu *et al.*, 2024), and elucidate the mechanistic basis of behavior (Dombrovski *et al.*, 2023; Shiu *et al.*, 2024). In vertebrates, neurons with similar functions can be scattered across regions, making it difficult to test proposed wiring schemes through sparse connectivity sampling from separate animals. A prime example is the zebrafish pretectum, where binocular and monocular neurons are intermingled in a non-topographic organization (Kubo *et al.*, 2014; Naumann *et al.*, 2016). Recent advances in functional connectomics in this model organism—combining in vivo calcium imaging with subsequent electron microscopy in the same animal—have made it possible to directly link functional neuronal activity with its underlying synaptic connectivity (Wanner and Friedrich, 2020; Friedrich and Wanner, 2021; Vishwanathan *et al.*, 2024). This approach offers unprecedented insights into how connectomic motifs support neuronal responses, sensory processing, and ultimately behavior in the vertebrate brain.

Here, to unravel the circuit-level mechanisms of sensory evidence accumulation, we applied functional connectomics to the zebrafish hindbrain. We reconstructed 84 functionally identified neurons and 165 synaptic partners. Cellular-resolution volumetric registration to a common reference brain and cross-modality comparisons enabled us to refine and explicitly test previously proposed connectivity motifs (Naumann *et al.*, 2016; Bahl and Engert, 2020; Dragomir, Štih and Portugues, 2020). Our findings highlight recurrent connectivity and interhemispheric inhibition as fundamental motifs for sensory evidence accumulation, a structure reminiscent of a line attractor (Seung, 1996; Khona and Fiete, 2022). Moreover, we identified ipsilateral disinhibitory inputs from a small population of transiently active neurons. We propose that this disinhibition motif may play a key role in endowing the network with the ability to respond to a rapidly changing sensory environment while maintaining its ability to slowly filter relevant cues from noisy signals.

We complement our electron microscopy dataset by a library of functionally identified cell morphologies obtained through a two-photon-guided labeling strategy. Using such detailed structure-to-function knowledge, we further train a classifier algorithm, allowing us to predict functional properties based on neuronal morphology only. This approach enhances the utility of previously acquired EM datasets by enabling connectomic analysis of sparse neuronal circuits even in the absence of calcium imaging. While in the past we had proposed a potential network structure of the anterior hindbrain purely based on functional imaging, we can now constrain models using ground truth structural information. Our updated network model reproduces the experimentally observed neuronal dynamics and makes explicit predictions for new experiments to further probe circuit structure and function. These advances not only deepen our mechanistic understanding of vertebrate sensory-motor transformations but also establish a general new framework for applying connectomics to diverse neural circuits across species.

Results

Correlative electron and light microscopy in a neural circuit performing motion integration

To explore the relationship between structure and function in the anterior hindbrain, we first identified neurons based on their functional dynamics using two-photon calcium imaging (**Fig. 1a**, (Bahl and Engert, 2020)). To that end we used 7 days post-fertilization (dpf) transgenic larvae expressing a nuclear calcium indicator (Dana *et al.*, 2019) under the *elavl3* pan-neuronal promoter and red markers in the main inhibitory neuronal subtype (Satou *et al.*, 2013) as well as in vascular endothelial cells (Fujita *et al.*, 2011), *Tg(elavl3:H2B-GCaMP7f, gad1b:DsRed, kdrl:mCherryCAAX)*. We recorded neuronal responses evoked by left- and rightward moving dots of 100% coherence in six optical planes spaced by 12 µm along the dorso-ventral axis in a region spanning from the medial optic tectum to the caudal hindbrain. We performed 2D segmentation of the time-averaged recordings using a convolutional neural network (Weigert *et al.*, 2020) to obtain neuron-specific masks (**Methods**). While many diverse neurotransmitter types exist (Higashijima, Mandel and Fetcho, 2004), the transgenic Gad1b+ label allowed us to assign inhibitory identity to cells, as GABA is the main inhibitory neurotransmitter in the zebrafish brain (Filippi, Mueller and Driever, 2014). Neurons displayed similar calcium dynamics as previously reported (**Extended Data Fig. 1a,** (Bahl and Engert, 2020)). Unbiased clustering revealed three main functional cell types. Based on their dynamics we named these cells motion integrator (MI), motion onset (MON), and slow motion integrator (SMI) neurons (**Fig. 1b**, **Extended Data Fig. 1a,b,** and **Methods**). Previously, we used labels based on the potential functional role of these cells (evidence integrator, dynamic threshold, and motor command neurons, respectively) during sensory-motor decision-making (Bahl and Engert, 2020). Out of 15017 functionally imaged neurons, we found 618, 108, and 339 neurons of each type, respectively with the largest fraction located in the anterior hindbrain (62%: 358, 24, and 275 neurons of each type, respectively, **Extended Data Fig. 1c** and **Methods**) but also located in the pretectum (Pt), midbrain

(Mb) and cerebellum (Cb) as well as other regions. Previous work suggests that the anterior hindbrain performs temporal integration of direction-selective pretectum whole-field motion inputs (Bahl and Engert, 2020). Compatible with these previous observations, we found that a large fraction of neurons in the anterior hindbrain were direction selective (DS) (75.6% of neurons had an absolute DS index>0.5, **Extended Data Fig. 1d)** with generally slower dynamics than their pretectum and midbrain counterparts (**Extended Data Fig. 1e**).

Using the same larva, we performed bilateral enucleation to facilitate fixative diffusion and enhance ultrastructure and extracellular space preservation followed by a modified rOTO (reduced osmium tetroxide-thiocarbohydrazide-osmium) EM staining protocol (Tapia *et al.*, 2012; Hua, Laserstein and Helmstaedter, 2015) (**Methods**). We identified the region containing most of the neurites of the functional neuronal types using sparse hindbrain electroporations (Boulanger-Weill *et al.*, 2017) and c3pa-GFP photoactivation (Förster *et al.*, 2018) (**Extended Data Fig. 2a,b**) in separate age-matched larvae. We also performed X-ray computed tomography to ensure staining homogeneity and tissue integrity, and target the sectioning to specific neuronal circuits (**Extended Data Fig. 2c–g**). We then collected 4010 coronal sections using an automated tape ultra-microtome (Hayworth *et al.*, 2014) and performed multi-beam scanning EM (mSEM) at 4 x 4 x ~30 nm resolution (~416 x 265 x 112 µm, spanning from the medial midbrain to rhombomere 3, **Fig. 1d**) totaling 51.4TB of imaging data (**Methods**). Volumetric nanometer-precise alignment and connectome reconstruction were performed via a series of largely automated workflows, enabling high-quality neuronal morphology reconstruction ((Turner *et al.*, 2022), **Methods**). To find single-cell correspondences between two-photon and EM imaging, we performed registration using manually placed corresponding landmarks ((Bogovic *et al.*, 2016), **Methods**). This strategy yielded single-cell precision registration even in dense, low-contrast regions of the brain (**Fig. 1e** and **Extended Data Fig. 2h**). Fluorescently labeled blood vessels—which were not used as landmarks for the registration—allowed us to independently confirm the quality of the mapping (**Extended Data Fig. 2h**). Finally, the EM and registered two-photon datasets were uploaded into an online browsing platform (Dorkenwald *et al.*, 2023), enabling collaborative proofreading of morphology and connectivity of functionally identified neurons (**Methods**).

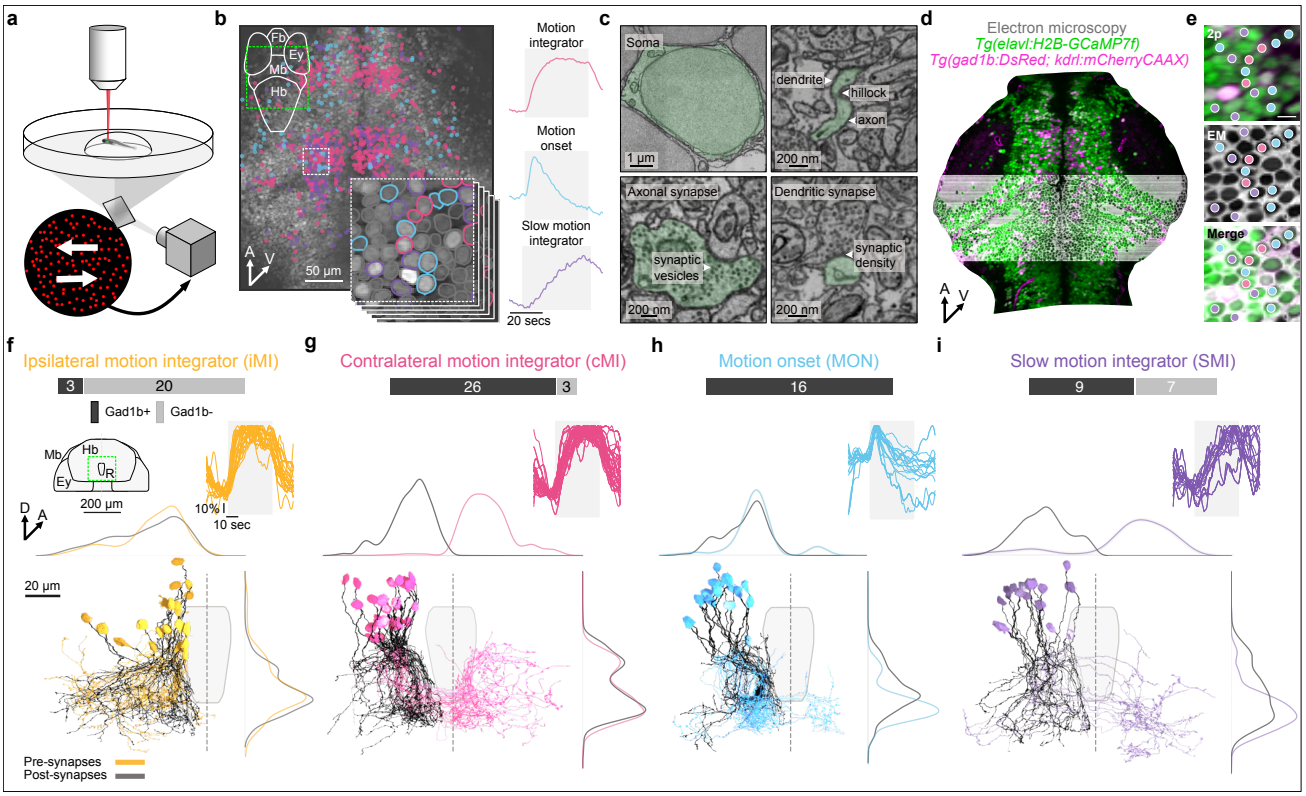

Fig. 1 | Correlative light and electron microscopy of neurons involved in motion evidence integration. a, Schematic of the two-photon imaging setup showing the bottom projection of coherently moving random dots. **b,** Left: spatial distribution of clustered neurons. The background grayscale image represents the average of the six functionally imaged planes. Top-left schematic shows coarse brain organization (dorsal-to-ventral view) and the location of the functionally imaged area (green dashed square). The white dashed square is magnified in the bottom-right snippets, which depict individual planes and are also shown in **(e).** Neurons are circled based on their functional types, while non-clustered neurons are circled in gray. Right: normalized K-means-based regressors used for neuron clustering. Stimulus consists of 0%, 100% (gray shaded area), and 0% coherence. **c,** EM ultrastructural details of a reconstructed neuron. **d,** Single plane of the two-photon image stack mapped to the EM dataset. Magenta shows inhibitory neurons (Gad1b+) and blood vessels (kdrl+). Green shows nuclear-localized GCaMP7f. Gray indicates the EM dataset. **e,** Detailed alignment between the two-photon imaging (2P) and EM datasets. Scale bar: 5 µm. Neurons from the clustered populations are indicated by colored dots. **f**, Structure-function relationship of functionally imaged and reconstructed neurons in tail-to-head view. Top: distribution of neurotransmitter identity shown as Gad1b-positive (likely inhibitory, black) or Gad1b-negative (presumably excitatory, gray). Left: schematic showing coarse brain organization and location of the reconstructed neurons below (green dashed square) surrounding outlines of the raphe (also shown below). Right: traces representing the normalized $\Delta F/F_0$ neuronal activity over time for motion in the preferred direction. Bottom: reconstructed ipsilateral motion integrator (iMI) neurons with somas and axons in orange and dendrites in black. The dashed line represents the midline. Surrounding plots are distributions of presynaptic (orange) and postsynaptic (black) synapses along the x (top) and y (right) axes. **g–i,** show identical representation for other neuron types. Abbreviations: Mb, midbrain; Hb, hindbrain; R, raphe; Ey, eye; A, anterior; D, dorsal; V, ventral. Neuron-type names, their abbreviations, and associated colors are used throughout the paper.

Structure-function relationship of functionally identified neurons

Stereotypy is a core feature of vertebrate and invertebrate brains, rooted in genetic templates and consistent environments. However, it varies among neighboring microcircuits, meaning that the brain is not strictly composed of homogeneous, repeating units (Silberberg, Gupta and Markram, 2002). Instead, a flexible template enables diverse microcircuits to meet distinct functional demands across brain regions both at the morphological and connectomic levels. For example, *Drosophila* neurons show stereotyped yet variable cell and synapse numbers across hemispheres (Bates *et al.*, 2020; Schlegel *et al.*, 2021), and human neurons show morphological diversity across brain regions, age and gender (Han *et al.*, 2023). In the zebrafish optic tectum, neurons with similar transcriptional profiles can vary in shape, connectivity, and visual responses (Shainer *et al.*, 2025) suggesting a weak structure-to-function relationship in this region. To explore this aspect in the anterior hindbrain we reconstructed 52 MI neurons, 16 MON neurons, and 16 SMI neurons (located in rhombomeres 1–3) and identified their neurotransmitter identity (**Fig. 1f–i** and **Extended Data Fig. 3a–d**). To probe the connectivity of functionally identified neurons we trained convolutional neural networks to automatically detect synaptic clefts and assign presynaptic and postsynaptic partner neurons ((Macrina *et al.*, 2021), **Methods** and **Extended Data Fig. 4a–f**).

All of these neurons were unipolar, with the axon emerging from a primary dendrite projecting ventrally, a structure reminiscent of invertebrate neurons (Dorkenwald *et al.*, 2024; Schlegel *et al.*, 2024). We observed distinct patterns among the different neuron types: ipsilateral-projecting MI (iMI) neurons were predominantly Gad1b- (20/23), while contralateral-projecting MI (cMI) neurons were mostly Gad1b+ (26/29). MON neurons were exclusively Gad1b+ and primarily contralateral-projecting (12/16), whereas SMI neurons exhibited a mix of neurotransmitter and projection types, including 4 ipsilateral-projecting Gad1b+ neurons and 12 contralateral-projecting neurons (9 Gad1b+ and 3 Gad1b-) (**Fig. 1f–i**). iMI neurons were generally positioned closer to the midline compared to other types, with overlapping axons and dendrites; some axons extended beyond the volume caudally, rostrally, or both (**Fig. 1f** and **Extended Data Fig. 3a**). In contrast, cMI neurons were located more lateral, displaying clustered dendrites adjacent to the raphe, and had only a few axons leaving the volume (**Fig. 1g** and **Extended Data Fig. 3b**). MON neurons showed tightly clustered dendrites and axons (**Fig. 1h** and **Extended Data Fig. 3c**) with the majority of axonal synapses located on the

ipsilateral side. SMI neurons had more dispersed dendrites and axons along both the dorso-ventral and rostro-caudal axes (**Fig. 1i** and **Extended Data Fig. 3d**).

To quantify neuronal similarity we computed the NBLAST scores within and in-between neuronal types using previously established methods (Costa *et al.*, 2016) and a zebrafish neuron-specific calibration (**Methods**). NBLAST enables the clustering of vertebrate and invertebrate neurons based on their position and local geometry (Costa *et al.*, 2016). We found that NBLAST scores were not consistently higher within functional types than across functional types (**Extended Data Fig. 3e,f**) indicating that this metric does not reliably predict function from morphology alone. In summary, aside from MON neurons, functionally defined neurons that contribute to motion evidence accumulation in larval zebrafish exhibit loose morphological stereotypy and diverse morphological identities.

Distinct connectivity motifs across functionally identified neurons in the anterior hindbrain

Starting with the 84 functionally identified neurons, we automatically identified a total of 3,218 post-synapses (inputs) and 2,126 pre-synapses (outputs) (**Methods** and **Extended Data Fig. 4a–e**). Among these, 9.59% of randomly selected connected segments were successfully reconstructed (dendrites leading to a soma, or axons leading either to a soma or to the edge of the volume), resulting in the identification of 165 additional partners: 38 truncated axons and 127 neurons that had not been functionally imaged (**Fig. 2a**). To investigate connectivity motifs we generated a connectivity matrix that included only functionally identified neurons (**Fig. 2b)** and complemented it with truncated axonal partners terminating within the volume (**Extended Data Fig. 4f**). Distinct connectivity patterns emerged for each neuron type, both at the input and output levels (**Fig 2b–j** and **Extended Data Fig. 4f–n**).

iMI neurons broadly targeted all functional types with a strong preference for MON neurons (35% of synapses, **Fig. 2c**). Notably, approximately 6% of the output synapses targeted iMI neurons, suggesting recurrent connectivity within this neuronal subtype. Additionally, a large fraction of the inputs originated from either the rostral end of the imaged volume or from cMI neurons (22% each, **Fig. 2d** and **Extended Data Fig. 4g**). Previous studies have demonstrated co-activation of anterior hindbrain and pretectum neurons during whole-field visual motion, supporting the existence of anatomical connectivity between these regions (Naumann *et al.*, 2016; Chen *et al.*, 2018). While contributions from other areas cannot be excluded, our findings are consistent with the idea that iMI neurons temporally integrate inputs coming from the pretectum and then relay such signals to other neuron types in the anterior hindbrain.

cMI neurons inhibited all functional types on the contralateral side except MON neurons with a strong bias towards iMI and cMI neurons (22% and 16% respectively, **Fig. 2e**). They received similar amounts of disinhibitory ipsilateral inputs from MON neurons on the ipsilateral side, caudal axonal inputs and disinhibitory inputs from cMI cells on the contralateral hemisphere (15%, 18% and 13% respectively, **Fig. 2f** and **Extended Data Fig. 4h**). These observations provide anatomical confirmation of predicted interhemispheric inhibition within the anterior hindbrain refining turning behavior by processing pretectal inputs (Naumann *et al.*, 2016).

MON neurons targeted cMI neurons ipsilaterally in a disinhibitory manner (18%, **Fig. 2g** and **Extended Data Fig. 4i**) and received mixed inhibitory and excitatory inputs originating from other cells within the anterior hindbrain (41%, **Fig. 2h** and **Extended Data Fig. 4i**).

SMI neurons predominantly targeted caudally projecting neurons with myelinated axons (35%, both ipsilaterally and contralaterally, **Fig. 2i** and **Extended Data Fig. 4j**), suggesting that this cell type might have a role in motor execution—as we have previously proposed (Bahl and Engert, 2020). Consistent with this, one excitatory ipsilateral SMI neuron targeted three Rov3 reticulospinal neurons (**Fig. 2i,** and **Extended Data Fig. 4j,o**), a subtype implicated in lateralized responses to whole-field

motion (Orger *et al.*, 2008). SMI neurons received the greatest diversity of inputs, in nearly equal proportions: rostral axonal inputs (12%), caudal axonal inputs (9%), excitation from iMI neurons (7%), ipsilateral inhibition from MON neurons (7%), and contralateral inhibition from cMI neurons (9%, **Fig. 2j** and **Extended Data Fig. 4j**). Interestingly, we did not find any statistical differences between pre- and post-synapses sizes across functionally identified cell types (**Extended Data Fig. 4p,q**), suggesting balanced functional connection weights (Holler *et al.*, 2021) across cell types in the anterior hindbrain.

In summary, our sparse connectomic reconstructions in the hindbrain support a network model of bilateral inhibition across hemispheres mediated by cMI neurons, ipsilateral disinhibition driven by MON neurons, recurrent connectivity within iMI neurons, and direct inputs from SMI neurons to reticulospinal neurons, which drive lateralized movements. To provide the broader scientific community with an online platform to browse neurons from connectomic analyses, we further developed an open-source atlas containing molecular labels and anatomic regions (**Extended Data Fig. 5**, (Vohra et al., in preparation)) to which we uploaded all reconstructed neurons and axonal segments (connected to functionally identified inputs and output partners).

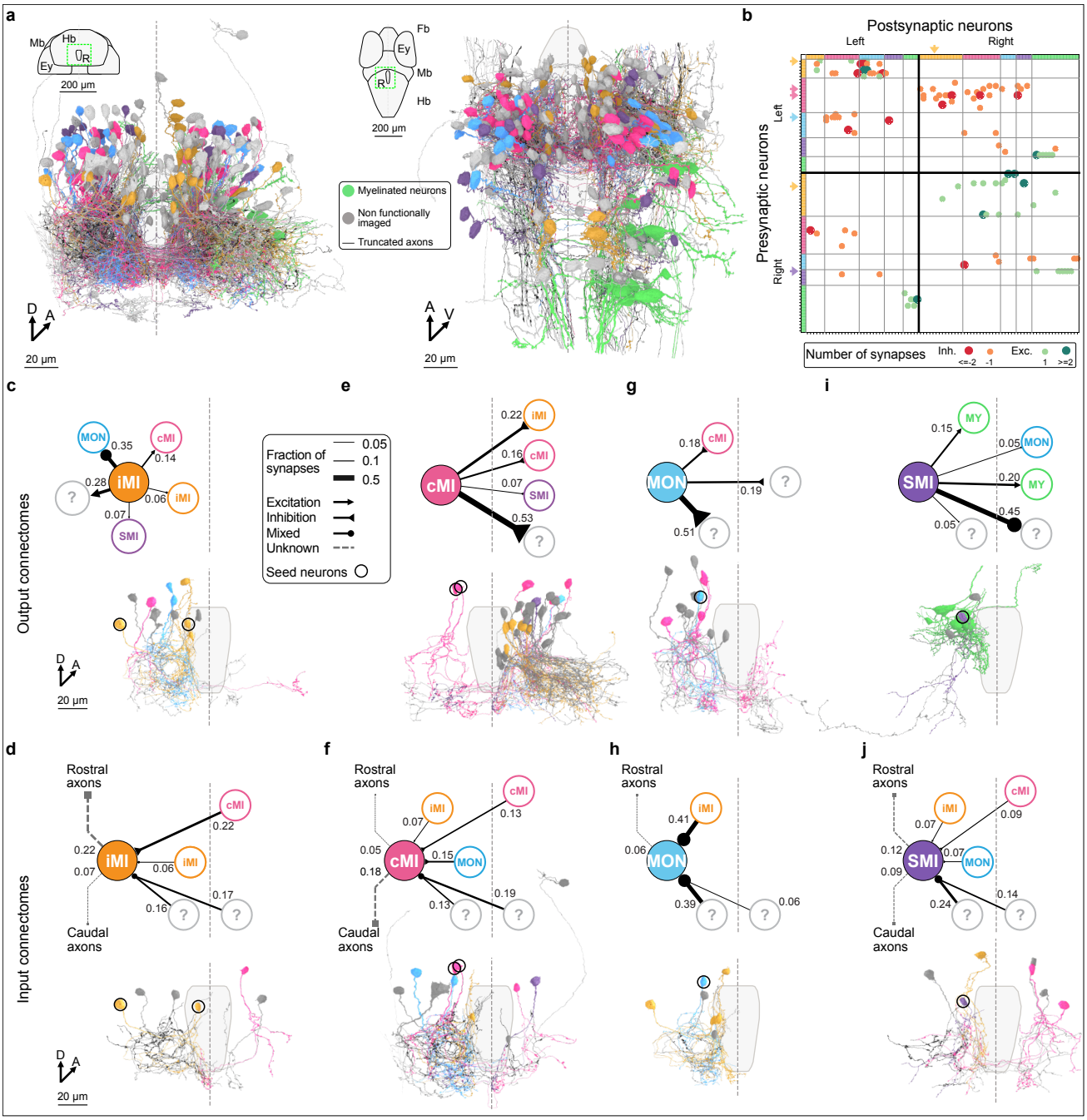

Fig. 2 | Connectomic analyses of functionally identified neuronal subtypes. a, All neurons reconstructed in this study: 84 functionally imaged neurons and connected partners: 38 truncated axons and 127 not functionally imaged neurons. Left panel: tail-to-head view, right panel: dorsal view. Top schematics show coarse brain organization and location of the reconstructed neurons below (green dashed square) surrounding outlines of the raphe (also shown below). **b,** Connectivity matrix with neurons sorted according to their functional types and hemispheres (thick black bars). Output (**c,e,g,i**) and input (**d,f,h,j**) connectomes. Top diagrams: Simplified connectivity motifs extracted from the connectivity matrix. Connections accounting for less than 5% of the total synapse number are not shown. Question marks represent non-functionally imaged neurons. The dashed line indicates the midline. Bottom: Representative example connectomes (tail-to-head view) for one or two seed cells. All neuronal parts (some, axon, and dendrites) are colored with the same color. Abbreviations: Mb, midbrain; Hb, hindbrain; R, raphe; Ey, eye; A, anterior; D, dorsal; V, ventral.

Two-photon-guided characterization of function, anatomy, and neurotransmitter identity

Many existing anatomical resources (Kunst *et al.*, 2019; Vishwanathan *et al.*, 2024) do not contain functional information about cell morphologies, limiting their usability for neural circuit dissections. Even for our CLEM dataset, time considerations during the initial two-photon imaging session limited

295 the acquisition of neural activity to only a few planes. Such data subsampling leads to a considerable
296 fraction of reconstructed partners for which functional information is missing. To assign functional
297 labels to these neurons, we sought to train classifiers to predict neuronal functional types based on
298 morphology. In the ideal situation, such classifiers may even be trained and tested purely based on
299 light microscopy experiments, providing a powerful strategy to enhance any, not just our current, EM-
300 and light-based library of anatomical reconstructions. Our CLEM dataset provides a unique ground
301 truth dataset for understanding the relationship between structure and function across anterior
302 hindbrain cell types, allowing us to rigorously validate such classifiers.

303 Using two-photon excitation of photoactivatable GFP (Patterson and Lippincott-Schwartz, 2002;
304 Förster *et al.*, 2018), we reconstructed the anatomy of functionally characterized neurons (Kramer *et*
305 *al.*, 2019). We combined this approach with *in-situ* RNA hybridization, HCR FISH (Choi *et al.*, 2018),
306 employing *gad1b* and *vglut2a* probes to selectively label GABAergic (inhibitory) and glutamatergic
307 (excitatory) neurons, respectively (**Fig. 3a**). This strategy was applied across 47 larvae to generate a
308 comprehensive multi-feature neuronal library that links functional dynamics, anatomy, and
309 neurotransmitter identity—purely based on light microscopy experiments (**Fig. 3b–e**). Neuron
310 functional types were determined through clustering analysis consistent with our CLEM experiment
311 (**Fig. 1b, Methods**). Remarkably, the patterns observed in these experiments closely mirrored results
312 from our CLEM dataset (compare **Fig. 3b–e** and **Extended Data Fig. 6a–d** with **Fig. 1f–i** and
313 **Extended Data Fig. 3a–d**), validating the two approaches across multiple animals and imaging
314 modalities.

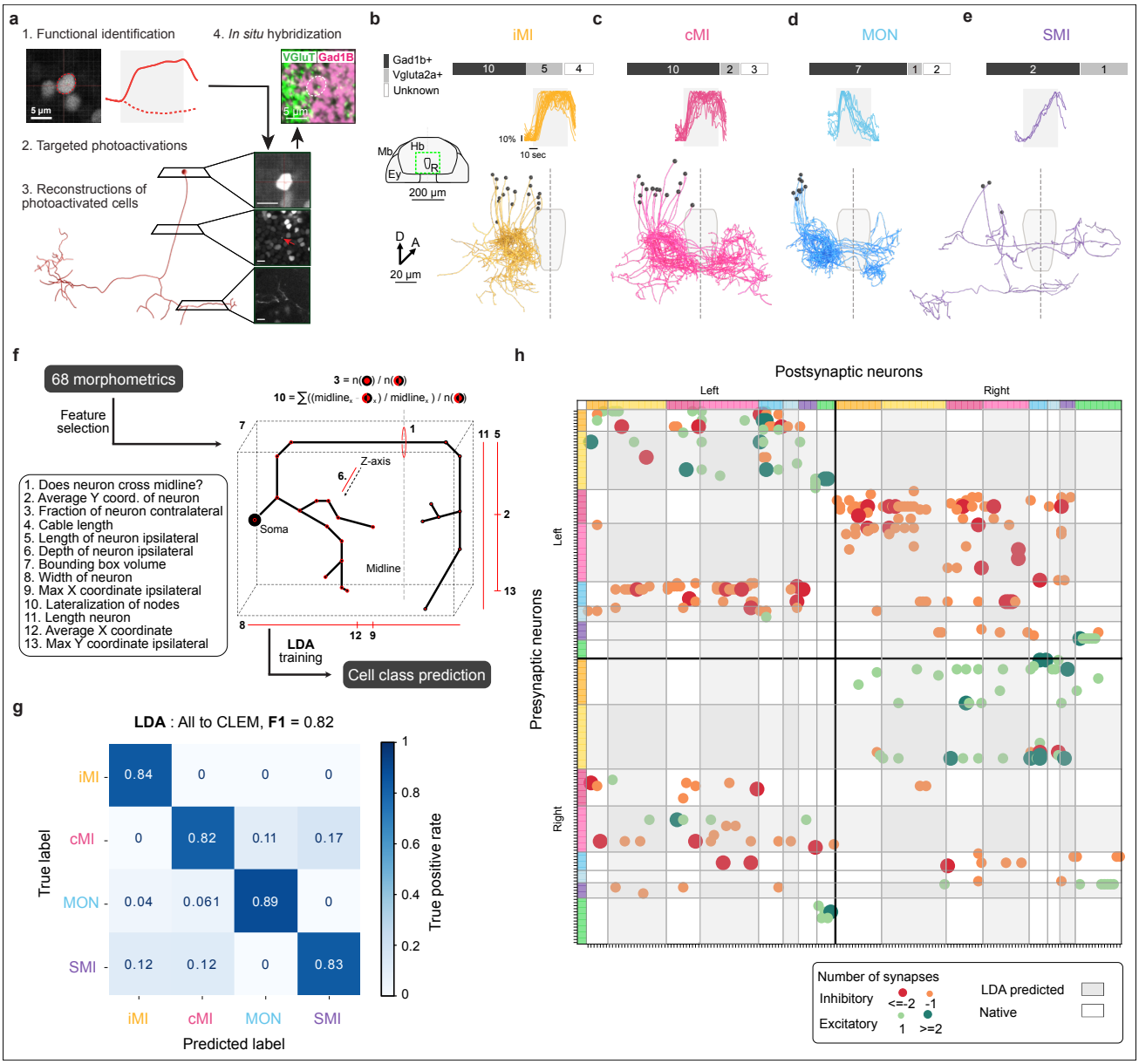

Fig. 3 | Single cell photoactivation and functional types predictions across datasets. a, Schematic of the functional identification process followed by single-cell photoactivation, *in situ* hybridization, and manual morphological reconstruction. **b,** Structure-function relationship of functionally imaged and photoactivated iMI neurons. Top: distribution of neurotransmitter identity shown as Gad1b-positive (black), Vglut2a-positive (gray) or unknown (white). Left: schematic showing coarse brain organization (tail-to-head view) and location of the reconstructed neurons below (green dashed square) surrounding outlines of the raphe (also shown below). Right: traces representing the normalized $\Delta F/F_0$ neuronal activity over time. Bottom: reconstructed iMI neurons with somas in black. The dashed line represents the midline. Abbreviations: Mb, midbrain; Hb, hindbrain; R, raphe; Ey, eye; A, anterior; D, dorsal; V, ventral. **c–e,** identical representation for other neuron types. **f,** Schematic of the features selection used for the linear discriminant analysis (LDA) to predict functional cell types. **g,** LDA confusion matrix of true positive rate using CLEM and photoactivated neurons as the ground truth and predicting CLEM cells. The prediction performance F1-score for the entire matrix is indicated in the plot title. **h,** Classifier-enhanced connectivity matrix of reconstructed EM neurons, sorted according to their functional types and hemispheres (thick black bars). The background of columns and rows of neurons whose functional type has been predicted through LDA are shaded in gray.

Structure-to-function classification

Our joint photoactivation and CLEM datasets comprise a library of 131 cells (42 iMI, 44 cMI, 26 MON, and 19 SMI), establishing a direct link between structure, function, and neurotransmitter identity. This dataset can serve as ground truth for training a classifier. Using a linear discrimination analysis

335 approach (LDA), we fitted a model that correlates morphological features with functional neuron type.
336 LDA is a statistical method used for dimensionality reduction and classification, identifying a linear
337 combination of features that optimally separates two or more classes by maximizing variance between
338 classes while minimizing variance within classes. Analysis of the model parameter contribution
339 (**Methods**) suggested that only a few metrics had strong predictive power (**Fig. 3f–g** and **Extended**
340 **Data Fig. 6e**, **Methods**). Applying a cross-validation holdout strategy (**Methods**), we achieved a
341 classifier predictive performance of 0.82 (F1-scores, **Fig. 3g**). This result indicates that our classifier
342 can reliably predict the functional type of a neuron based solely on its morphology, even for cells it
343 had not encountered during training. We further tested the classifier's performance with smaller
344 datasets, using cells from either the photoactivation experiments or our CLEM library. We still
345 achieved predictive performance above 0.74 (F1-scores, **Extended Data Fig. 6f**). Remarkably, when
346 training our classifier only on photoactivated cells and testing it on our CLEM ground truth library, we
347 maintained an F1-score of 0.76 (**Extended Data Fig. 6f**). These findings demonstrate that a classifier
348 exclusively trained on light microscopy experiments can provide a generalizable, powerful, and cost-
349 effective method for functionally labeling neurons in morphological libraries where functional imaging
350 is absent, largely benefiting our current EM dataset, as well as other existing resources. We
351 benchmarked our approach against other established methods (Li *et al.*, 2017; Choi, Kim and Hyeon,
352 2023) and found that our method consistently outperformed them in predictive accuracy (**Extended**
353 **Data Fig. 6g–i**).

354

355 **Enhancing the CLEM dataset**

356 A direct application of this approach is the enhancement of our correlated light and EM dataset. Within
357 this dataset, we identified 108 pre- and postsynaptic reconstructed unmyelinated neurons that we had
358 not functionally imaged during our initial two-photon session (**Fig. 1a, Fig. 2a**). Using our trained
359 classifier, we predicted the functional types of 78.7% of the non-functionally imaged neurons,
360 considerably enriching our library with additional labels, which allowed us to further populate the
361 synaptic connectivity matrix of the anterior hindbrain (**Fig. 3h** and **Extended Data Fig. 7a–i**). Notably,
362 the overall connectivity arrangement remained almost identical, confirming that our original dataset
363 contains a representative subset of functionally imaged cells. These results also indicate that our
364 classifier can generate similar conclusions about the structure and function relationship of neural
365 networks compared to what is achievable with CLEM.

366

367 **An anatomically and functionally constrained circuit model of a flexible neural integrator**

368 We had previously proposed a neural circuit arrangement of the anterior hindbrain, in which temporal
369 integration of motion evidence may be implemented via recurrent connectivity of integrator cells.
370 These cells, we suggested, compete with a transiently active pool of inhibitory neurons, together
371 initiating swimming decisions when excitation overcomes inhibition (Bahl and Engert, 2020). While in
372 our previous model, we speculated about connectivity purely based on functional imaging, we now
373 have detailed ground truth connectivity information by the identified EM connections of functionally
374 identified cells (**Figs. 2** and **3**). To keep our new model tractable, we focused our analyses on the
375 major contributors within the circuit, only considering identified connections constituting at least 10 %
376 of the input or output synapses (**Fig. 2c–j** and **Extended Data Fig. 7**). We assigned excitatory and
377 inhibitory labels based on the observed majority of connection types (**Figs. 1f–i** and **3b–e**). The
378 resulting network connectivity matrix (**Fig. 4a**), allowed us to draw a putative circuit arrangement of
379 the anterior hindbrain involved in the integration of visual motion cues and sensory-motor control (**Fig.**
380 **4b**). Key elements of this circuit arrangement are recurrent connectivity of excitatory iMI neurons
381 (iMI^+), implementing the temporal filtering of incoming input signals from the pretectum, delayed
382 feedforward inhibition of MON cells, via inhibitory iMI neurons (iMI^-), disinhibition of inhibitory cMI cells

(cMI⁻) via MON neurons, as well as interhemispheric inhibition via cMI⁻ cells. Based on the identified axons projecting from the rostral part into the circuit (**Extended Data Fig. 7a**), we modeled input to the circuit as excitatory connections from the pretectal region onto iMI⁺ and MON.

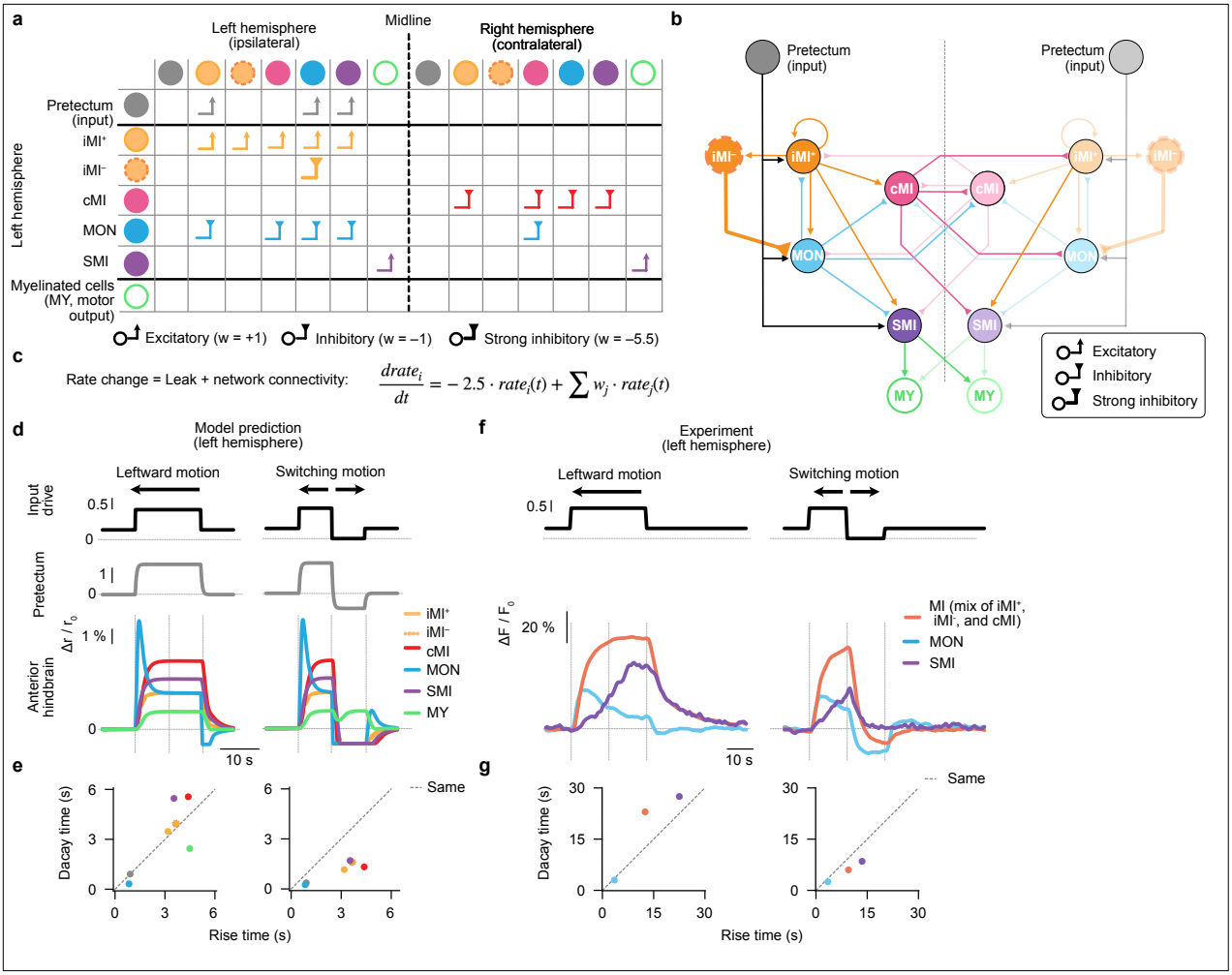

Fig. 4 | A connectome-constrained neural network model of the anterior hindbrain. a, Summary matrix of all identified connections with at least 10 % connectivity probability, based on our CLEM analyses. For simplicity, only connections originating on the left hemisphere are displayed. For neurons on the right hemisphere, the matrix is identical. Excitatory and inhibitory connections are indicated by arrowheads and triangles, respectively. **b,** Network model following the same connection scheme as in **(a)**. **c,** Differential equation for neuron *i*. The full model contains 14 units (7 on each hemisphere, **Methods**), following connectivity weights w_j shown in **(a)**, with equivalent leak factors (–2.5) across all cell types. **d,** Simulation results for two different stimulus configurations (leftward motion, left plot; switching motion, right plot). The input drive represents the stimulus direction on the left eye (positive for leftward motion, and slightly below baseline for rightward motion). Gray and colored lines indicate the dynamics of units on the left hemisphere. Responses on the contralateral hemisphere are in **Extended Data Fig. 8a**. **e,** Rise and decay times (**Methods**) of cell types for different stimulus configurations. When the direction suddenly changes for the switching motion stimulus (right plot), integrator cells turn off more rapidly than if the motion just stops (left plot). **f**, New two-photon imaging experiment following visual stimulation protocol in (**d**), showing average traces for each functional cell type (trial-, fish-, and cell-averaged, n=4 fish, 2 planes per fish, and 12 trials per plane). **g,** Same as in **(e)**, but for experimental data. Decay dynamics of MI and SMI are faster for the switching motion stimulus (right plot) compared to when motion just stops (left plot).

In principle, the weight of all identified connections (= 144), the passive membrane biophysics, such as its leak constant (= 14)—or even complex activity-dependent conductances and plasticity features—of each cell type may be free model parameters and could be tuned to obtain the experimentally observed dynamics. We wanted to know to what extent a model behaves where these parameters are largely fixed. Given the observed equal distribution of synapse sizes (**Extended Data**

Fig. 4p,q), we chose the same weights in the network across cell types (see **Methods** for parameter choice). Assuming that all cells have the same membrane properties, we chose identical leaks across the network. Model simulations revealed dynamics resembling the ones observed in experiments (compare **Fig. 4d**, left with **Figs. 1f–i** and **3b–e**): For leftward motion, integrator cells in the left hindbrain had slower onset and offset dynamics than neurons in the simulated pretectum and MON neurons showed their characteristic transient response at the start of motion. On the contralateral hemisphere, model integrator cells showed clear motion opponent inhibition, with MON neurons rebounding at stimulus offset, also matching experiments (compare **Extended Data Figs. 8a** and **1f**, and (Bahl and Engert, 2020)). We further quantified the relationship between onset and offset dynamics for each cell type (**Fig. 4e**, left), revealing a mostly linear relationship, as expected from integrators with low-pass filter dynamics. The good qualitative agreement between our CLEM-constrained network model and our imaging data adds confidence that the proposed connectivity structure may indeed represent an important functional circuit motif in the anterior hindbrain.

After showing that our model can match the known activity dynamics in the anterior hindbrain, we sought to further challenge and validate our model by explicitly testing some of its predictions on new experimental data. We presented the model with a stimulus in which motion direction abruptly changes from leftward to rightward motion—a configuration that we had not previously used when developing our experimental and modeling pipelines (**Fig. 4d**, right). Our model predicted a rapid state-switching across hemispheres upon direction change, with faster offset dynamics than if motion just stops (compare **Fig. 4e**, left, and right). We next probed these predictions via two-photon imaging (**Fig. 4f**). We presented larvae with the same stimuli as in our model and classified neurons based on the response dynamics to the stimulus continuously moving in one direction (same regressors as in **Fig. 1b**, **Methods**). The location of resulting cell types in the brain resembled the known distribution pattern (compare **Extended Data Fig. 8d** and **Fig. 1b**). Across stimuli, response dynamics in the experiment closely resembled model predictions. Quantification of onset and offset times (**Fig. 4g**) showed that MI neurons turn off faster for switching motion, compared to when motion just stops, hence also agreeing with our model predictions (**Fig. 4e**).

Based on our circuit model, we further argued that the inhibitory signal of the transiently active MON cells on the contralateral side (**Extended Data Fig. 8a**) at such transition points may be responsible for the observed dynamics. Its transient activation via pretectal input may rapidly release inhibition via cMI neurons, thus switching off the contralateral hemisphere. To test these ideas, we used our model to clamp the activity rates of MON neurons on both hemispheres to zero (**Extended Data Fig. 8b**). Such an experiment would be challenging to do in real larval brains, given the number and sparse distribution of MON cells. Model manipulation with silenced MON neurons predicted faster integration across the network. It also largely abolished the difference between onset and offset times (**Extended Data Fig. 8c**), suggesting that MON neurons indeed seem to mediate these dynamics.

In summary, we find that our CLEM-constrained circuit model of the anterior brain can reproduce our experimentally observed dynamics of motion-sensitive cells in the anterior hindbrain. When motion direction abruptly changes, which is a realistic situation in natural environments, our model proposed that MON neurons allow the system to rapidly switch states, flexibly endowing the circuit with both slow integration capabilities and fast response times.

Discussion

In this study, we combined functional calcium imaging and electron microscopy to elucidate the circuit architecture underlying sensory evidence accumulation in the larval zebrafish anterior hindbrain. Although this dual approach has already been used (Briggman, Helmstaedter and Denk, 2011; Lee *et al.*, 2016; Vishwanathan *et al.*, 2017; Bae *et al.*, 2018; Wanner and Friedrich, 2020) we demonstrate its feasibility in a large inter-hemispheric vertebrate brain network (**Fig. 1**). Moreover, we use CLEM

as a tool to test and update existing hypothetical circuit models with anatomical information, which we then validate with new experiments. This allows us to refine existing hypotheses (Bahl and Engert, 2020; Dragomir, Štih and Portugues, 2020) regarding how neuronal connectivity supports the accumulation of visual motion cues over time.

Our findings provide the first mechanistic insights into how evidence accumulation of noisy visual motion cues is implemented within a recurrent neural network at the synaptic level. We identify interhemispheric inhibition and recurrent connectivity as key motifs of this circuit, a structure reminiscent of a line attractor (Seung, 1996; Khona and Fiete, 2022) (**Fig. 2**). Additionally, the presence of strong bilateral inhibitory interactions (including reciprocal inhibition), mediated by contralateral motion integrator neurons (cMIs) confirms previous predictions obtained in this region (Naumann *et al.*, 2016; Bahl and Engert, 2020) based solely on calcium imaging. These interactions were proposed to explain behavioral statistics of zebrafish larvae responding to whole-field motion. Reciprocal inhibitory connectivity has also been shown to underlie ring attractor networks encoding head direction in both vertebrates and invertebrates (Turner-Evans *et al.*, 2020; Petrucco *et al.*, 2023), raising the possibility that similar connectivity motifs contribute to sensory integration in the hindbrain. For example, cyclically connected populations of caudal hindbrain neurons contribute to persistent activity in neurons controlling horizontal eye movements (Vishwanathan *et al.*, 2024). While denser reconstructions may yet reveal such cyclic structures within the anterior hindbrain, our findings suggest that different motifs serve complementary roles in supporting persistent neuronal activity. Understanding how these motifs are specialized for their respective motor outputs will require further investigation. Our findings also complement earlier studies identifying rhombomere 1 of the hindbrain as an integrator of multiple sensory inputs such as luminance or gaze direction (Wolf *et al.*, 2017; Petrucco *et al.*, 2023). Whether the motion-sensitive neurons identified in this study may also integrate other sensory variables remains an open question.

We also demonstrate that MON neurons receive a mixture of excitatory and inhibitory inputs from two types of feed-forward connected iMI cells. Although the calcium dynamics were not sufficiently fast to disentangle the difference in onset time constant between these two populations, we propose that these neurons together provide first excitation and then delayed inhibition onto MONs, generating a transiently active activity pattern in these cells upon motion onset. A similar di-synaptic arrangement has been shown to generate fast, gated activity dynamics in the larval Xenopus visual system (Akerman and Cline, 2006). We also demonstrate that MON neurons provide strong ipsilateral inhibitory input to cMI neurons in an unexpected disinhibitory arrangement. Finally, our findings further support the idea that SMI neurons act as the final readout of the evidence accumulation process, directly targeting reticulospinal neurons responsible for executing movement. The strong, stereotyped connectivity between SMI neurons and caudal-projecting reticulospinal neurons aligns with previous studies demonstrating that these neurons drive laterally biased motor outputs (Orger *et al.*, 2008).

Linking neural morphology with function has long been a major challenge in vertebrate connectomics, but recent advances have successfully achieved this in the mouse visual cortex (The MICrONS Consortium *et al.*, 2021; Ding *et al.*, 2023). In our study, we trained and validated a classifier that predicts functional neuron types based solely on their anatomical features (**Fig. 3**). This approach significantly expands the utility of connectomic datasets, allowing functional inference in electron microscopy volumes where direct calcium imaging is not available. This validation provides strong support for the notion that functionally distinct neuronal populations exhibit conserved morphological features, at least within the anterior hindbrain of zebrafish. Future applications of this approach could extend to other brain regions and species, accelerating the functional annotation of large-scale connectomic datasets.

Finally, we incorporated our anatomical findings into a computational model of sensory integration, constrained by the observed connectivity patterns and neurotransmitter identities. By minimal tuning

of connection weights and biophysical parameters, we demonstrated that our network model circuit could reproduce the experimentally observed dynamics of our measured cell types in the anterior hindbrain. The success of this model suggests an unexpected functional role of MON neurons in enabling fast responses to abrupt transitions in visual stimulation direction – a situation that frequently occurs in the naturalistic environment of animals (**Fig. 4**). The identified circuit arrangement in the anterior hindbrain may thus endow animals with a robust, yet flexible, system that can slowly filter important signals from noise and, at the same time, supports the rapid resetting of sensory integrators to allow fast reactions to external stimuli. Traditionally, disinhibitory connectivity in the motor system has been understood as a mechanism for movement initiation. Indeed, in the basal ganglia, disinhibition releases the thalamus and brainstem from suppression, allowing motor commands to propagate to the cortex and muscles (Lanciego, Luquin and Obeso, 2012).

It remains unclear how individual neurons' biophysical properties as well as synaptic strengths are shaping the dynamics observed in our analysis. For example, our model could not reproduce the observed slower ramping dynamics in SMI neurons, nor their trial-to-trial variability (Bahl and Engert, 2020). We also required the inhibitory inputs from iMIs to be increased to generate the correct MON neuron dynamics, potentially suggesting specific receptor types in these cells. Future experiments using voltage recordings, electrophysiology, transcriptomic analyses, and selective ablations could further refine our understanding of how such circuits are implemented. Recent analyses of *Drosophila* connectomes have integrated biophysical measurements to refine circuit models (Ammer *et al.*, 2023; Shiu *et al.*, 2024), an approach that remains largely unexplored in zebrafish. Measuring the biophysical properties of individual neuron types will be essential for further constraining network models and understanding the computational principles underlying sensory-motor transformations (Bargmann and Marder, 2013).

The connectomes and analysis tools presented here are openly available to the community and linked to an integrated atlas of the zebrafish brain. Our dataset provides a comprehensive view of vertebrate hindbrain circuitry in the zebrafish, complementing existing connectomic resources, including reconstructions spanning rhombomeres 4 to 8 (Vishwanathan *et al.*, 2024) of the ocular motor integrator system (Vishwanathan *et al.*, 2017), and whole-brain EM volumes (Svara *et al.*, 2022; Petkova, Januszewski, et al., *in prep.*). Our light-microscopy-trainable classifier enables functional inference in electron microscopy volumes without requiring calcium imaging, providing a scalable, cost-effective approach for circuits tested across a wide range of experimental paradigms. Our strategy will accelerate high-throughput functional annotation of vertebrate brain networks, enabling further dissections of the computational principles underlying sensory-motor decision-making. More broadly, our findings lay the groundwork for applying connectomics to diverse neural circuits, bridging the gap between structure and function in the vertebrate brain.

Methods

Zebrafish

For the correlative light and EM experiment (CLEM, **Figs. 1** and **2**) we generated a triple transgenic *Tg(elavl3:H2B-GCaMP7f*$^{+/+}$*, gad1b:dsRed*$^{+/-}$ (Satou *et al.*, 2013)*, kdrl:mCherryCAAX*$^{+/-}$ (Fujita *et al.*, 2011)*)* larva obtained by crossing adult transgenic *Tg(elavl3:H2B-GCaMP7f, gad1b:DsRed)* and *Tg(elavl3:H2B-GCaMP7f, kdrl:mCherryCAAX)* lines in nacre background, *mitfa*$^{-/-}$ (Lister *et al.*, 1999) yielding high GCaMP7 fluorescence. The *Tg(elavl3:H2B-GCaMP7f)*^{u344Tg} transgenic line was generated using standard methods (Dowell *et al.*, 2024). We raised small groups of 20–30 larvae in filtered fish facility water in Petri dishes (9 cm in diameter) on a 14 h light, 10 h dark cycle at a constant 28 °C. From 4 dpf onwards, we fed larvae with paramecia once per day. The experiment was performed on 7 dpf larvae. For sparse cell electroporations (**Extended Data Fig. 2a**), we incrossed

551 *Tg(elavl3:H2B-GCaMP7f)*^{u344Tg} lines and selected offspring based on green fluorescence. For the area
552 photoactivation (**Extended Data Fig. 2b**), we incrossed *Tg(alpha-tub:c3pa-GFP*$^{+/-}$*)*^{a7437Tg} (Bianco *et*
553 *al.*, 2012) with *Tg(elavl3:H2B-GCaMP6s*$^{+/-}$*)*^{jf5Tg} (Freeman *et al.*, 2014) adults and selected offspring for
554 green fluorescence. Animals were 7 dpf and 6 dpf old, respectively. For the combined functional
555 recordings, single-cell photoactivation, and HCR FISH staining experiments (**Fig. 3**), we outcrossed
556 *Tg(alpha-tub:c3pa-GFP*$^{+/-}$*; elavl3:h2b-GCaMP6s*$^{+/-}$*)* and *Tg(alpha-tub:c3pa-GFP*$^{+/-}$*)*^{a7437Tg} adults,
557 selecting for larvae that are homozygous for *c3pa-GFP* and heterozygous for *h2b-GCamp6s*. For the
558 imaging experiment after our model prediction (**Fig. 4g**), we used incrossed *Tg(elavl3:GCaMP8s)*, a
559 newly generated line expressing *GCaMP8s* in neurons. To generate the line, we injected the Tol2
560 vector transgene construct (Tol2-elavl3:GCaMP8s (Zhang *et al.*, 2023)), obtained from Janelia
561 Research Campus, and transposase RNA into 1–4-cell-stage embryos. We then isolated transgenic
562 lines by screening for high expression of bright green fluorescence in the central nervous system in
563 the next generation. For the experiments shown in **Figs. 3** and **4g** experiments, larvae were raised in
564 E3 water on a 14 h light, 10 h dark cycle at a constant 28 °C without feeding. All experiments were
565 approved by the Harvard University and Konstanz University committees on the use of animals in
566 research and training.

567 **Visual stimuli**

568 All visual stimuli during functional imaging consisted of ~1,000 dots (2 mm in diameter) moving at 1.8
569 cm s^{-1}, projected (60 Hz, P300 Pico Projector, AAXA) from below through mildly light-scattering
570 parchment paper. Dots were shown in red on a black background to minimize interference of the
571 visual stimulus with the functional GCaMP imaging. To ensure that the animals did not track individual
572 dots to detect motion, each dot had a short lifetime (200 ms mean) and stochastically disappeared
573 and immediately reappeared at a random location within the arena. One stimulation trial consisted of
574 40 s of 100% coherent motion either drifting leftward or rightward, interleaved by 20 s of 0% coherence
575 before and after. For the CLEM experiment (**Fig. 1**), we also presented moving sine gratings drifting
576 leftward or rightward, but did not include these stimulus trials in our analysis. For the imaging
577 experiments in **Fig. 4g**, we presented animals with 30 s of 100 % coherence, with motion either
578 running continuously or abruptly switching direction after 15 s. Stimuli across trials were interleaved
579 with 40 s of 0% coherence. In all experiments, stimuli were shown in a random sequence.

580 **Two-photon calcium imaging and analysis**

581 The larva was fully embedded in a drop of agarose (UltraPure Low Melting Point Agarose, Invitrogen),
582 at ~35 °C at the center of a Petri dish (9 cm in diameter, VWR). After the agarose was solidified the
583 dish was filled with fish facility water and transferred into the measurement chamber of a custom-built
584 two-photon microscope, operated by custom-written Python 3.7-based software (PyZebra2P). We
585 used a femtosecond-pulsed laser (MaiTai Ti:Sapphire, Spectra-Physics) equipped with a set of x/y-
586 galvanometers (Cambridge Technology), a 20x infrared-optimized objective (XLUMPLFLN, Olympus)
587 to scan over the brain and two photomultipliers (green and red) amplified by two current preamplifiers
588 (SR570, Stanford) to collect fluorophores emissions. We used frame acquisition rates of around 1 Hz.
589 Laser power was measured to be ~13 mW at the specimen. Such power levels did not interfere with
590 behavior in previous tail-free imaging experiments (Bahl and Engert, 2020). During functional imaging,
591 the laser was tuned to 950 nm to collect GCaMP7f fluorescence. We sequentially imaged six planes
592 spaced at 12 µm, centered on the anterior hindbrain region (336 x 336 µm at 0.48 x 0.48 µm
593 resolution). In each plane, we showed from 2 to 9 visual stimulation trials. Immediately after the
594 experiment, we anesthetized the fish by replacing the water with a 0.015% MS-222 (Sigma-Aldrich)
595 solution in fish facility water. This procedure enabled us to acquire an additional motion artifact-free
596 high-resolution stack at 1020 nm excitation (420 x 420 x 90 um at 0.6 x 0.6 x 2 µm resolution) with
597 simultaneous collection of GCaMP7f and DsRed fluorescence. The total imaging session lasted ~5
598 hours.

599 Activity recordings of each plane were first motion-corrected using NoRMCorre (Pnevmatikakis
600 and Giovannucci, 2017) and temporally averaged. We used a convolutional neural network
601 segmentation approach (StarDist) to perform high-accuracy segmentation of the nuclei in each plane
602 (Weigert and Schmidt, 2022). Calcium dynamics for each nuclei mask were then extracted as $\Delta F/F_0$
603 traces using Python numpy array slicing. K-means clustering of functional cell types was performed
604 on pooled activity traces from the CLEM experiment (**Fig. 1**) and all reconstructed neurons from our
605 targeted photoactivations experiments (**Fig. 3**). The elbow method (Umargono, Suseno and S. K.,
606 2019) suggested 4 functionally distinct clusters. These clusters were further isolated by two
607 successive K-means clustering steps with 3 and 2 target clusters as parameters. The first iteration
608 isolated MON dynamics, fast motion integrator dynamics (MI-1), and a third, slower group. The
609 second iteration performed on this slower population revealed an additional motion integrator group
610 (MI-2) as well as a slow motion integrator group (SMI). Thus, our clustering approach yielded 4
611 neuronal clusters with distinct temporal dynamics. For all cells in each cluster, we computed the
612 average rise time until neuronal activity reaches 90% of the maximal response, revealing a clear
613 separation of timescales across clusters (**Extended Data Fig. 1b**, only showing CLEM cells). We then
614 computed 3 final regressors by pooling neurons belonging to the MI-1 and MI-2 clusters and averaging
615 the activity of all neurons belonging to each clustered population. Neurons in the CLEM recording
616 were then assigned to one of the 3 functional types by computing the correlation coefficient with
617 individual regressors. Neurons whose correlation coefficient with a regressor was larger than 0.8 and
618 that had a response of at least 20 % $\Delta F/F_0$ were assigned to the corresponding functional type. All
619 other neurons remained unassigned.

620 Direction selectivity indexes (**Extended Data Fig. 1f**) were computed using standard methods
621 (Boulanger-Weill *et al.*, 2017):

622 $$DSI = \frac{\max(R_R) - \max(R_L)}{\max(R_R) + \max(R_L)},$$

623 where $max(R_R)$ and $max(R_L)$ are the maximal $\Delta F/F_0$ response values during the entire rightward
624 and leftward stimulation. Negative responses were set to 0.

625 In the imaging experiments presented in **Fig. 4g,** we used our newly generated fish line
626 *Tg(elavl3:GCaMP8s)***.** As GCaMP8s is expressed in the cytosol of cells we had to adjust the
627 segmentation parameters. We employed cellpose3 (Stringer and Pachitariu, 2025) to segment
628 neurons based on the time-averaged imaging stack, tuned to the following parameters for the
629 standard cyto3 model: cell diameter = none; follow threshold = 0.7; cellprob threshold = –0.4; lower =
630 0; upper = 90.0, which generated very good segmentation results across the brain (**Extended Data**
631 **Fig. 8d**). We then computed $\Delta F/F_0$ time traces from the resulting masks and used the same regressors
632 and cell type classification strategy as for our other imaging experiments (**Figs. 1** and **3**). We then
633 averaged all labeled cells per group to obtain response dynamics. For the continuous motion stimulus,
634 we computed the time until neuronal activity reaches 90% of the maximal response during the time
635 window of 30 s after motion onset. We chose the activity at the end of the stimulation period to
636 compute the time until activity decayed to 10 % of that value. For the switching motion stimulus, we
637 used the 15 s time point as a reference using the same approach.

638

639 **<u>Sparse electroporations and area photoactivations</u>**

640 Sparse electroporations were performed as in (Boulanger-Weill *et al.*, 2017). Briefly, 4 dpf larvae were
641 embedded in a droplet of agarose and anesthetized with 0.015% MS-222 (Sigma-Aldrich) in fish
642 water. The agarose next to the anterior hindbrain was removed using a microsurgical blade. The
643 electroporations were performed under a fixed-stage upright microscope equipped with a long working
644 distance objective (10x UPlanFL N 10X/0.30na, Olympus). The silver wire microelectrode and bath

electrode were mounted on micro-manipulators with the microelectrode holder containing an additional side port to apply air pressure with a syringe. Borosilicate glass capillaries (1.2 mm outer diameter, 0.68 mm inner diameter, with filament by World Precision Instruments) were pulled using a pipette puller (PC-10, Narishige, set at 68/58 °C) to obtain a 1 µm tip diameter. Pipettes were filled with 2 µL of cmv:lyn-tdTomato plasmid DNA solution and inserted into the anterior hindbrain of larvae. The lyn tag enables high-efficiency targeting of the red fluorescent protein to the cell's membrane and is thus ideal for studying neuronal morphology (Kunst *et al.*, 2019). Following optimized protocols (Zou, Friedrich and Bianco, 2016), two or three stimulation bursts (around 0.5 s per burst, consisting of 2 ms pulses at 200 Hz at 28 V were delivered using a square pulse stimulator (Sd9, Grass Technologies) and monitored using digital oscilloscope (TDS 2014, Tektronix). After the electroporations, larvae were freed from the agarose and kept isolated for 2 days. At 6 dpf, we then performed two-photon functional imaging of GCaMP6s (see previous section) to measure the response dynamics of the labeled cells to random dot motion. For subsequent morphological imaging of electroporated cells, we then anesthetized the fish and imaged at 1030 nm to collect dual-color z-stacks at high spatial resolution (0.46 x 0.46 x 1.5 µm) of both GCaMP and td-Tomato. Morphological imaging data was filtered (3D Gaussian blur, sigma 1.0 in x, y, and z) in Fiji (Schindelin *et al.*, 2012). Labeled neurons were then semi-automatically traced with the open-source reconstruction software neuTube (Feng, Zhao and Kim, 2015), using default settings and optimal node resampling. We then saved cells as .swc files. Using the GCaMP6s channel we then generated a transform per larva, allowing us to map reconstructed electroporated cells to a reference brain (Randlett, Wee, E. A. Naumann, *et al.*, 2015).

For area photoactivation (**Extended Data Fig. 2b**), fish were anesthetized with 0.015% MS-222 (Sigma-Aldrich), and c3pa-GFP was photoactivated using cycles of 40 short pulses of 200 ms at 1 Hz at a laser wavelength of 750 nm, following established protocols (Kramer *et al.*, 2019). After 1–3 initial trial pulses to check whether any adjacent cells were photoactivated and to readjust the region of interest if necessary, the whole protocol consisting of 15 cycles was executed, with five-minute intervals between two activation cycles. Photoactivation was targeted over a 50 x 40 µm region containing neurons with motion integration dynamics in the anterior hindbrain.

Sample preparation for the EM imaging

For the CLEM experiment, we used a protocol modified from (Tapia *et al.*, 2012) to enhance extracellular space preservation which improves synapse detection (Pallotto *et al.*, 2015) and permits single-cell resolution imaging using X-ray tomography. Unless noted, all steps were performed at room temperature (RT). Immediately after the two-photon stack acquisition, the larva, was still anesthetized and embedded in agarose. We replaced the water with a dissection solution (64 mM NaCl, 2.9 mM KCl, 10 mM HEPES, 10 mM glucose, 164 mM sucrose, 1.2 mM $MgCl_2$, 2.1 mM $CaCl_2$, pH 7.5) supplemented with 0.02% tricaine (Hildebrand *et al.*, 2017). We then cut small slits in the agarose to expose the eyes and performed bilateral enucleations to enhance extracellular space preservation and heavy metal staining. We used a custom-made hook that was carefully inserted behind the eyes to prevent brain damage. The larva was immediately transferred to a fixation solution at 4°C (2.5% glutaraldehyde, 0.1M cacodylate buffer supplemented with 4.0% mannitol at pH 7.4). Cacodylate buffer: 0.3M sodium cacodylate, 6mM CaCl2, pH 7.4. To improve the fixation, the tissue was rapidly microwaved (cat. no. 36700, Ted Pella, equipped with a power controller, steady-temperature water recirculator, and cold spot) in the fixative solution (this step lasted <5 min after initial transfer into fixative). The microwaving sequence was performed as in (Tapia *et al.*, 2012): at power level 1 (100 W) for 1 min on, 1 min off, 1 min on then to power level 3 (300 W) and fixed for 20 s on, 20 s off, 20 s on, three times in a row. Fixation was then continued overnight at 4°C in the same solution. The following day, the sample was then washed again in 0.5x cacodylate buffer (3 exchanges, 30 min each before osmication (2% OsO_4 in 0.5x cacodylate buffer, 90 min). After a quick wash (< 1 min) in 0.5x cacodylate buffer the sample was reduced in 2.5% potassium ferrocyanide in

694 0.5x cacodylate buffer for 90 min then washed with filtered H_2O (3 exchanges, 30 min each) and then
695 incubated with 1% (w/v) thiocarbohydrazide (TCH) in filtered H_2O (and filtered with a 0.22 µm syringe
696 filter before use) for 45 min to enhance staining (Hua et al., 2015). Due to poor dissolution of TCH in
697 water, the solution was heated at 60 °C for ~90 min with occasional shaking before filtering and then
698 placed at RT for 5 min before the incubation step. The sample was then washed with filtered H_2O (3
699 exchanges, 30 min each) before the second osmication (2% OsO_4 in filtered H_2O, 90 min) and then
700 washed again (3 exchanges, 30 min each). Then, en-bloc staining was performed overnight using 1%
701 uranyl acetate in filtered water at 4 °C. The solution was sonicated for 90 min and filtered with a
702 0.22um syringe filter before use. Steps involving uranyl acetate were performed in the dark. The
703 following day, samples were then washed with filtered H2O (3 exchanges, 30 min each). Next, the
704 samples were dehydrated in serial dilutions of ethanol (25%, 50%, 75%, 90%, 100%, 100% for 10
705 min each step) and then in propylene oxide (PO) (100%, 100%, 30 min, each step). Infiltration was
706 performed using LX112 epoxy resin with BDMA (21212, Ladd) in serial PO dilution steps, each lasting
707 4h (25% resin/75% PO, 50% resin/50% PO, 75% resin/25% PO, 100% resin, 100% resin). Samples
708 were mounted in fresh resin in a mouse brain support tissue (Hildebrand *et al.*, 2017) with the head
709 exposed to facilitate cutting and prevent the sample from sinking to the bottom of the resin molds.
710 Mouse tissue was fixed using standard procedures (Fang et al., 2018) and then cut into 2–3 mm wide
711 cubes which were pierced using a puncher (0.75 mm, 57395, EMS) to insert the larva. The cubes
712 were stained along with fish samples using the protocol described above except that the uranyl
713 acetate overnight step was performed at RT. The samples were then cured with support tissue for 3
714 days at 60°C. For all steps, a rotator was used. Aqueous solutions were prepared with water passed
715 through a purification system (Arium 611VF, Sartorius Stedim Biotech). The protocol lasted 5
716 consecutive days including surgery, fixation, staining, and resin embedding followed by 3 days of
717 resin curing.

718 **X-ray computed tomography**

719 To achieve high contrast X-ray and mSEM imaging we sequentially optimized OsO_4 staining duration,
720 X-ray imaging, and voltage and performed deep learning-based X-ray reconstruction (**Extended Data**
721 **Fig. 2e,f**). The OsO_4 staining was optimized first in previous batches of samples to yield the mSEM
722 staining protocol described previously. The imaging voltage and post-processing were optimized in
723 the main sample described in this study. In total this sample was imaged for ~300 hours which did not
724 interfere with mSEM imaging. For each sample, the block was trimmed to expose the head of the fish
725 for imaging (Xradia 520 Versa, ZEISS). To assess the imaging quality, we computed a modified
726 version of Michelson's contrast that was robust to noise at multiple sections along the main axis of
727 the larvae:

728 $$\text{Contrast} = \frac{I_{\max} - I_{\min}}{I_{\max} + I_{\min}}$$

729 Where I_{max} and I_{min} are the average intensity values over the 80th and below the 20th percentile
730 respectively. We also computed the signal-to-noise ratio (SNR) at the same locations according to
731 (Joy, 2002). X-ray tomography stacks were post-processed using a deep neural network product
732 included in the Xradia software.

733 **Sample sectioning and mSEM image acquisition**

734 After X-ray imaging, the block was re-embedded in resin and cured for 3 days at 60 °C and trimmed
735 in a diamond shape (Hildebrand *et al.*, 2017). 4010 sections ranging from 30 to 35 nm were
736 automatically collected on carbon-coated tape using a custom tape collection device (ATUM)
737 (Hayworth *et al.*, 2014) mounted to a commercial ultramicrotome. The tape was cut into strips and
738 deposited on 30 silicon wafers that were post-stained (Hildebrand *et al.*, 2017). Wafers were then
739 mounted on the 61-beam mSEM stage (MultiSEM 505, ZEISS) and each section's position was
740 determined using a reflected light microscope to guide the high-resolution imaging. Imaging was

741 performed at 4 x 4 nm pixel resolution using secondary electron emission using a dwell time of 400
742 ns per pixel. The quality of each section was assessed using previously described methods (Shapson-
743 Coe *et al.*, 2024).

744 **mSEM image alignment, stitching, rendering, neuronal morphology proofreading**

745 We trained convolutional neural networks to detect defects and classify locations that contain tissue
746 for each montaged section. We used self-supervised convolutional neural networks to generate dense
747 displacement fields between sections (Popovych *et al.*, 2024), and then hierarchically minimized the
748 elastic energy in the set of all displacement fields to produce an aligned image. We created an "image
749 mask" that contained defects and locations that were classified as misaligned. We trained
750 convolutional neural networks that we used to segment cells, detect synaptic clefts, compute their
751 sizes, and assign presynaptic and postsynaptic objects from the cell segmentation at each cleft
752 (Macrina *et al.*, 2021). Cell segmentation and synapse detection and assignment used the aligned
753 image with locations in the "image mask" set to black. We refined the detection of synaptic clefts and
754 reduced false positives by visually inspecting two dendrites and one axon and classified predicted
755 synapses as true positive, false positive, and identified false negative missing synapses (**Extended**
756 **Data Fig. 4b-d**). We performed a Receiver Operating Characteristic (ROC) curve analysis to establish
757 a size threshold that minimizes false positives (**Extended Data Fig. 4e**). This analysis determined
758 that a synapse size threshold of 44 voxels effectively excluded 90% of the false positive synapses,
759 providing a reliable criterion for refining the dataset and improving prediction accuracy. Finally, cell
760 segmentation was ingested into the ChunkedGraph proofreading system so that morphological errors
761 could be manually corrected, and synapses were ingested into an annotation table for consistent
762 analysis (Dorkenwald *et al.*, 2023).

763 **Multimodal, reference brain registrations and cell type determination**

764 Matching of neuronal identities from the 2P functionally imaged planes to the EM volume was
765 performed in two successive manual steps using the Fiji plugin Bigwarp (Bogovic *et al.*, 2016). We
766 first manually registered functional imaging planes to a higher z-resolution two-photon image stack
767 (z-steps = 2 µm, containing green and red fluorescence) using manually selected 844 landmarks. The
768 SNR of this stack was enhanced using content-aware image restoration (Weigert *et al.*, 2018). We
769 then registered this higher resolution two-photon image stack to a downsampled mSEM stack (0.512,
770 0.512, 0.480 µm/pixel) using manually selected 771 landmarks. This EM stack was downloaded from
771 Neuroglancer (https://github.com/google/neuroglancer) using Cloudvolume (Silversmith *et al.*, 2022).
772 These two registration steps generated two deformation fields which were successively applied to the
773 2P functionally imaged planes using Bigwarp (in linear deformation mode) and manually checked
774 exhaustively. The segmented neuronal masks were also deformed using these two steps (in nearest
775 neighbor mode). Deformed planes of green and red fluorescence (8-bit image stacks) and segmented
776 masks were uploaded to Neuroglancer using Cloudvolume enabling collaborative reconstruction and
777 cell type determination of the neurons of interest. To determine whether neurons were inhibitory, we
778 manually traced a mask surrounding the neuron's nuclei in the green channel and computed the
779 average corresponding red fluorescence. Neurons with values superior to 10 % of the maximum red
780 signal (25 in 8-bit scale) were considered inhibitory. Regions containing k-means clustered neurons
781 (**Extended Data Fig. 1c**) were determined by automatically registering the 2P functionally imaged
782 planes to the z-brain reference brain (Randlett, Wee, E. A. Naumann, *et al.*, 2015) using ANTs
783 (Avants, Tustison and Johnson, 2015). For regional annotations, we downloaded anatomical masks
784 from the mapzebrain atlas platform (Kunst *et al.*, 2019) and mapped them into the z-brain coordinate
785 system (Randlett, Wee, E. A. Naumann, *et al.*, 2015) using ANTs (Avants, Tustison and Johnson,
786 2015).

787 Finally, neurons traced in Neuroglancer were downloaded using Navis (Schlegel *et al.*, 2025) and
788 automatically registered to the z-brain reference brain (Randlett, Wee, E. A. Naumann, *et al.*, 2015).

789 To register cells from our downsampled mSEM stack to the z-brain reference brain, we manually
790 selected 207 landmarks in the mSEM stack and the *Tg(elavl3:H2B-RFP)* confocal stack in the z-brain
791 coordinate system to generate a bridge transform via Fiji Bigwarp. All neurons presented in this paper
792 have been registered to the z-brain reference brain (Randlett, Wee, E. A. Naumann, *et al.*, 2015) and
793 are available on our online platform.

794 **Two-photon photoactivation and neurotransmitter identity of functionally identified cells**

795 We selected larvae for green fluorescent nuclear expression and embedded animals in a droplet of
796 low-melting point agarose in a Petri dish with a diameter of 6 cm. The fluorescence of the H2B-
797 GCaMP6s makes the identification of c3pa-GFP difficult – at this stage, c3pa-GFP is not yet
798 photoactivated and thus very dim. To enable screening for c3pa-GFP, we initially performed a brief
799 activation experiment in the two-photon microscope, labeling a small region in the dorsal rostral
800 tectum. We only continued with the animals that showed some sign of tectal photoactivation patterns
801 after a maximum of 5 rounds of photoactivation. Morphologies originating from this area largely
802 remained local and did not overlap with the photoactivated neurons in the hindbrain. In a few cases,
803 neurons descended into the anterior hindbrain neuropil, coming close to the photoactivated cells but
804 did not interfere with our tracing. To accommodate larvae to the experiment and minimize motion
805 artifacts and plane shifts during imaging, we initially presented animals for 15 minutes with random
806 dot motion before starting the functional characterizations.

807 To quickly identify cell types, we then imaged a single plane in the anterior hindbrain for 15 – 30
808 minutes while presenting random dot motion. Using a custom-written Python script, we aligned
809 recordings to the onset of motion and averaged stacks across trials. Using Fiji (Schindelin et al., 2012)
810 we defined a small movable region of interest with the size of a cell to manually explore the stack for
811 neuronal dynamics matching the known cell type dynamics (Bahl and Engert, 2020). This analysis
812 step took less than 5 minutes per fish.

813 For each identified cell we then conducted targeted photoactivation at 760 nm. Using a custom-
814 written scanning waveform generator in PyZebra2P, we used a small activation spiral (less than 0.5
815 µm in diameter) focused onto the center of the nucleus of the cell. Due to the point spread function of
816 our microscope (~1 µm along the horizontal plane, and ~4 µm along the vertical axis), we were able
817 to activate c3pa-GFP in the cytosol without affecting neighboring neurons. Following recent protocols
818 (Kramer *et al.*, 2019), we used short activation pulses of 200 ms in length and 100 ms interpulse
819 interval. The required laser power at the specimen and the pulse counts for effective photoactivation
820 varied widely across fish. Some fish only required as few as 20 pulses (ca. 6 seconds) at 5 mW to
821 activate cells, whereas other fish often required up to 1000 pulses (ca. 5 min) at 8 mW. We attribute
822 this difference to variations in expression levels as some experimental fish are heterozygous and
823 some fish are homozygous for c3pa-GFP.

824 Following successful photoactivation, we anesthetized the fish by replacing the water in the Petri
825 dish with a 0.015% MS-222 solution. After 15 minutes of anesthesia, we then imaged a high-resolution
826 stack (100 planes, 0.4 µm x 0.4 µm x 2 µm; 90 s per plane) of the hindbrain and midbrain to capture
827 as much of the photoactivated cell's neurite morphology as possible. This step took around 2.5 hours
828 per animal.

829 To determine the neurotransmitter identity of the labeled cell, we performed HCR RNA-FISH (Choi
830 *et al.*, 2018) on the same fish immediately after the imaging session. To this end, we cut out a small
831 block of agarose containing the anesthetized fish and directly fixed the sample in ice-cold 4% PFA for
832 12–16 hours overnight at 4 °C. We then followed recent protocols optimized for zebrafish larvae
833 (Shainer *et al.*, 2023). We used probe sets against *gad1b* (probe set size 30, #NM_194419.1) and
834 *vglut2a* (*slc17a6b*, probe set size 20 #NM_001128821), with B1 and B2 amplifiers, respectively. We
835 used the B1-546 amplifier fluorophore and the B2-405 amplifier fluorophore, thus fluorescently
836 labeling *gad1b*-positive cells in red and *vglut2a*-positive cells in blue.

837 After the procedure, we placed the still agarose-embedded fish into the same two-photon
838 microscope where it had been imaged before. The PFA fixation and HCR RNA-FISH protocol
839 considerably reduced the fluorescence of a photoactivated c3pa-GFP cell. Cells were still identifiable
840 because they were slightly more fluorescent than neighboring non-photoactivated neurons. Neurites
841 in the photoactivated cells were however not visible anymore after the procedure. To further validate
842 the identity of the cell, we used landmarks such as the arrangement of neighboring nuclei or neuropil
843 structures with distinguishable distances to the labeled cells. We acquired two separate high-
844 resolution volume scans around the photoactivated cell body. Our custom-built microscope can only
845 simultaneously image green and red fluorescence or green and blue fluorescence, with a manual
846 replacement of a filter cube in the collection optics path between imaging sessions. As we acquired
847 green fluorescence in both sessions, we could identify our target cells in both imaging stacks to extract
848 the expression levels of both *gad1b* and *vglut2a* within the cytosolic ring around the nucleus. Labels
849 were largely exclusive to each other, allowing us to confidently assign neurotransmitter identity based
850 on which label was stronger. We labeled cells where both *gad1b* and *vglut2a* signals were
851 indistinguishable from background fluorescence as 'undefined'.

852 The custom-designed two-photon microscope used for these experiments was largely similar to
853 the one explained above used for the CLEM experiment. However, this system used a tunable MaiTai
854 ® DeepSee (Spectra-Physics) laser source with a built-in pre-chirp unit, a Nikon 25x Objective (N25X-
855 APO-MP), and a more sensitive Hamamatsu GaAsP PMT (H16201P-40-S3) for the green channel.
856 These features significantly improved the imaging quality of green signals and later facilitated the
857 reconstruction of photoactivated neurons. Reconstructions were performed in Fiji using the SNT semi-
858 automated tracing tool (Arshadi *et al.*, 2021).

859 **Zebrafish-optimized NBLAST probability matrix**

860 We used NBLAST (Costa *et al.*, 2016) to compute a matrix of morphological similarity of cells within
861 our CLEM dataset (**Extended Data Fig. 3e**). One of the major functions of the NBLAST algorithm is
862 the 2-dimensional scoring matrix (10 x 21) which provides a raw score of whether two neurons belong
863 to a similar cell type. The row of the scoring matrix represents the dot product of the tangent vectors
864 whereas columns represent the range of distances in micrometers. The default matrix is derived from
865 a dataset of *Drosophila* neurons and is sensitive to several factors, including dataset type, neuron
866 size, preprocessing methods, and the volume analyzed. To match the algorithm to our data, we
867 computed a zebrafish-optimized scoring matrix using the CLEM dataset. The training of such a matrix
868 requires matching and nonmatching sets of neurons (Costa *et al.*, 2016). We used our four functionally
869 and morphologically distinct cell types (iMI, cMI, MON, SMI) as matching sets. Non-matching sets of
870 neurons are drawn randomly from our CLEM dataset. The consistency of the matrix is assured by
871 using the n-fold (n=4). The detailed method and further advancements are provided in an upcoming
872 atlas paper (Vohra et al., *in preparation*).

873 **Morphology-based prediction of neuronal functional types**

874 With the unique availability of two ground truth datasets of structure and function relationship (**Fig. 1**
875 and **Fig. 3**), we sought to employ and train a classifier to predict a functional cell type based on
876 anatomical structure. Such a classifier will be useful for predicting functional response properties of
877 cells in anatomical libraries for which functional imaging has not been performed, including existing
878 EM reconstruction databases. To this end, first mapped all reconstructed neurons to a common
879 reference atlas (Randlett, Wee, E. a Naumann, *et al.*, 2015), using custom-written Python scripts and
880 ANTs (Avants, Tustison and Johnson, 2015). For neurons originating from the CLEM experiment (**Fig.**
881 **1**), we applied the same Bigwarp-based generated ANTs transforms that we used to map cell bodies
882 into the reference brain (see section above). For neurons originating from the two-photon guided
883 photoactivation experiments (**Fig. 3**), we used the h2b-GCaMP6s channel to generate a transform
884 between each stack against the corresponding reference stack.

885 Reconstructed neurons from the CLEM experiment were downloaded as high-resolution geometry
886 (.obj) files. These files are simple text files containing a list of surface vectors describing volumetric
887 meshes, allowing us to apply our ANTs transforms to map geometries into the z-brain coordinate
888 system. Using the *skeletor* package and the TEASAR algorithm (Sato *et al.*, 2000) in Python, we
889 skeletonized .obj files to 1.5 µm spacing and saved results as .swc files. This procedure ensured that
890 all neurons originating from different experiments and modalities ended up in the same coordinate
891 system with the same spatial tracing resolution, a prerequisite for the development of our classifier.

892 As our NBLAST matrix does not show a clear separability of cell types, we decided to build our
893 classifier using a feature-based approach. To this end, we exhaustively extracted 68 morphometrics
894 from each skeletonized neuron (**Extended Data Table 1**). All features were normalized by subtracting
895 the mean and scaling to unit variance across cells. To identify the most relevant of these features for
896 predicting functional cell types, we first selected feature subsets of different sizes. To this end, we
897 conducted feature ranking with reverse feature elimination using *sklearn.feature_selection.RFE* in
898 Python with "AdaBoostClassifier" as the learning estimator. For a given target feature subset size (1
899 – 68), the algorithm starts at the maximum number of features (68). It then uses the specified
900 estimator to evaluate the importance of features by fitting the model and then iteratively removes the
901 least significant feature until it reaches the desired target feature subset size. For each resulting
902 feature subset, we then extracted a predictive F1-score of how these features could be used to classify
903 cell types. Specifically, we split our cells (including both data from the CLEM and photoactivation
904 experiments) in a ratio of 70% train and 30% test. As a classifier algorithm, we chose Linear
905 Discriminant Analysis (LDA) with solver 'lsqr' (least squares solution). Performing the LDA training
906 and prediction step 100 times with different randomly selected training and test sets, allowed us to
907 compute the predictive F1-score as a function of the feature subset size (**Extended Data Fig. 6e)**.
908 We then selected the feature combination with the highest predictive performance as the final feature
909 set (**Fig. 3f**). We used this feature subset for all further cell type classifications.

910 Many cells identified through our pre- and post-synaptic connectomic reconstructions had their
911 soma in regions that were not covered by our 2P multi-plane imaging session. To compute the
912 performance of our classifier when predicting the functional type in such cases, we performed a 'leave
913 one out cross-validation' step on our ground truth datasets. To assess the quality of the classifier
914 using maximal and cross-modality training data, we combined both the CLEM and photoactivation
915 experiments. We iteratively chose one of our known CLEM cells and trained our classifier on all
916 remaining ground truth cells. Comparing the classifier prediction of the left-out CLEM cell with its true
917 functional type, allowed us to compute a confusion matrix, indicating the probability that a functional
918 prediction of a given EM cell is correct (**Fig. 3g**). We finally repeated the training on all available
919 ground truth cells (data from the CLEM and photoactivation experiments) to generate the final
920 classifier used to predict the functional response properties of EM cells that we had not imaged (**Fig.
921 3h**). Our trained cell type classifier should be applicable to also enhance other morphological
922 resources, containing anatomical reconstructions of neurons in the larval zebrafish anterior hindbrain.

923 Notably, the LDA classifier will place any target cell, even when it looks completely different from
924 the training dataset, into one of our defined 4 categories. To rule out such incorrect predictions, we
925 identified outliers within the predicted cells' morphometric features using an isolation forest algorithm
926 (*sklearn.IsolationForest*) and the local outlier factor (*sklearn.LocalOutlierFactor*). We trained these
927 outlier removal methods with the morphometric features of our functionally identified cells from both
928 the CLEM and photoactivation experiments.

929 We finally compared our morphology-based neuronal type prediction method to previously
930 established approaches (Li *et al.*, 2017). To do so, we computed persistence vectors and their
931 sampled versions (Li *et al.*, 2017) for each neuron using *navis.persistence_vectors* and trained a
932 linear discriminant analysis classifier (*sklearn.LinearDiscriminantAnalysis*) to predict functional types
933 (**Extended Data Fig. 6g, h**). Similarly, we calculated form factors (Choi, Kim and Hyeon, 2023) for

each neuron using *navis.form_factor* and trained another linear discriminant analysis classifier to predict functional types (**Extended Data Fig. 6i**).

Network modeling

We simulated the network model of the anterior hindbrain via an array of 14 first-order coupled differential equations (7 cell types on each hemisphere). We fed stimulus input drives into the first processing layer (pretectum) on the left and right sides, respectively. Input drives had a baseline activity of 0.5. A stimulation level of 100% random dot motion coherence to the left was simulated as increasing the input drive on the left by +1, and reducing it by 0.5 on the right side (**Fig. 4d**). For motion to the right, the input drive was adjusted accordingly. We did not attempt to build a biophysically realistic network model of the pretectum (Kubo *et al.*, 2014; Naumann *et al.*, 2016; Wang *et al.*, 2019). The activity was then further processed in the interhemispheric anterior hindbrain network. To keep the model simple and parameter space low, we fixed excitatory weights to +1, and inhibitory weights to –1. Because we found the connection between iMI⁻ and MON to be prominent in our data (**Extended Data Fig. 7a,b**), we here used a stronger inhibitory weight of -5.5. We modeled all cells with the same leak factor of –2.5, without assuming any specific biophysical features across the network. (**Fig. 4c**). Smaller leak factors than this value led to unstable network behaviors. Larger leak values led to overall faster dynamics. As our experimental measurement relies on GCaMP8s calcium imaging (**Fig. 4c**)—which represents a largely low-pass filtered version of the true neuronal activity—we did not aim to quantitatively match the time scales between the model and experiment. The self-recurrency of iMI neurons effectively reduced the leak of this cell type, explaining the slower integration dynamics compared to the input from the pretectum. Many neurons in the network model inherit these dynamics, explaining the overall slower temporal dynamics in the hindbrain. We used the Euler method (time step dt = 0.01 s). The full model follows these rules to update the firing rates:

Left hemisphere:

$$d\mathrm{PI}_l^+ = -2.5 \cdot \mathrm{PI}_l^+ + \mathrm{Stim}_l(t)$$
$$d\mathrm{iMI}_l^+ = -2.5 \cdot \mathrm{iMI}_l^+ + 1.0 \cdot \mathrm{PI}_l^+ + 1.0 \cdot \mathrm{iMI}_l^+ - 1.0 \cdot \mathrm{MON}_l^- - 1.0 \cdot \mathrm{CMI}_r^-$$
$$d\mathrm{iMI}_l^- = -2.5 \cdot \mathrm{iMI}_l^- + 1.0 \cdot \mathrm{iMI}_l^+$$
$$d\mathrm{CMI}_l^- = -2.5 \cdot \mathrm{CMI}_l^- + 1.0 \cdot \mathrm{iMI}_l^+ - 1.0 \cdot \mathrm{MON}_l^- - 1.0 \cdot \mathrm{CMI}_r^- - 1.0 \cdot \mathrm{MON}_r^-$$
$$d\mathrm{MON}_l^- = -2.5 \cdot \mathrm{MON}_l^- + 1.0 \cdot \mathrm{PI}_l^+ + 1.0 \cdot \mathrm{iMI}_l^+ - 5.5 \cdot \mathrm{iMI}_l^- - 1.0 \cdot \mathrm{MON}_l^- - 1.0 \cdot \mathrm{CMI}_r^-$$
$$d\mathrm{SMI}_l = -2.5 \cdot \mathrm{SMI}_l + 1.0 \cdot \mathrm{PI}_l^+ + 1.0 \cdot \mathrm{iMI}_l^+ - 1.0 \cdot \mathrm{MON}_l^- - 1.0 \cdot \mathrm{CMI}_r^-$$
$$d\mathrm{MY}_l = -2.5 \cdot \mathrm{MY}_l + 1.0 \cdot \mathrm{SMI}_l + 1.0 \cdot \mathrm{SMI}_r$$

Right hemisphere:

$$d\mathrm{PI}_r^+ = -2.5 \cdot \mathrm{PI}_r^+ + \mathrm{Stim}_r(t)$$
$$d\mathrm{iMI}_r^+ = -2.5 \cdot \mathrm{iMI}_r^+ + 1.0 \cdot \mathrm{PI}_r^+ + 1.0 \cdot \mathrm{iMI}_r^+ - 1.0 \cdot \mathrm{MON}_r^- - 1.0 \cdot \mathrm{CMI}_l^-$$
$$d\mathrm{iMI}_r^- = -2.5 \cdot \mathrm{iMI}_r^- + 1.0 \cdot \mathrm{iMI}_r^+$$
$$d\mathrm{CMI}_r^- = -2.5 \cdot \mathrm{CMI}_r^- + 1.0 \cdot \mathrm{iMI}_r^+ - 1.0 \cdot \mathrm{MON}_r^- - 1.0 \cdot \mathrm{CMI}_l^- - 1.0 \cdot \mathrm{MON}_l^-$$
$$d\mathrm{MON}_r^- = -2.5 \cdot \mathrm{MON}_r^- + 1.0 \cdot \mathrm{PI}_r^+ + 1.0 \cdot \mathrm{iMI}_r^+ - 5.5 \cdot \mathrm{iMI}_r^- - 1.0 \cdot \mathrm{MON}_r^- - 1.0 \cdot \mathrm{CMI}_l^-$$
$$d\mathrm{SMI}_r = -2.5 \cdot \mathrm{SMI}_r + 1.0 \cdot \mathrm{PI}_r^+ + 1.0 \cdot \mathrm{iMI}_r^+ - 1.0 \cdot \mathrm{MON}_r^- - 1.0 \cdot \mathrm{CMI}_l^-$$
$$d\mathrm{MY}_r = -2.5 \cdot \mathrm{MY}_r + 1.0 \cdot \mathrm{SMI}_r + 1.0 \cdot \mathrm{SMI}_l$$

with $rate(t) = rate(t-1) + drate \cdot dt$. We prevented negative activity rates by setting values to zero, whenever they became negative in the updating loop. To generate the activity rate plots in **Fig. 4d**, we computed rates relative to baseline (averaging 10 s before motion onset), matching our imaging analysis of fluorescent data for better comparisons between model and experiment. To

compute rise times, we measured the delay to 90% of the maximal rate per cell type. To compute decay times, we picked the value at the end of the stimulation period and computed the delay until the signal reached 10 % of this value. In the MON silencing experiment (**Extended Data Fig. 8b**), we clamped $\mathrm{MON}_l^-(t) = 0$ and $\mathrm{MON}_r^-(t) = 0$.

Data availability

All neurons described in this paper are browsable in FishExplorer: https://fishexplorer.zib.de/sandbox/.

Github code: https://github.com/arminbahl/Hb_structure_function

Funding

A.B. and F.K. were supported through the Emmy Noether Program (BA 5923/1-1), the Zukunftskolleg Konstanz, as well as the German Excellence Strategy (EXC 2117-422037984). J.B.W., F.K., G.F.P.S, F.E., and J.W.L. received funding from the Institutes of Health U19 Program (U19NS104653 and 1R01NS124017-01). J.B.W. received funding from the Philippe Foundation Inc. F.E. was also supported by the Simons Foundation (SCGB 542973 and NC-GB-CULM-00003241-02). G.F.P.S received funding from the Swiss National Science Foundation (Fellowships P2EZP3_188017 and P500PB_203130).

Author contributions

Project conceptualization: J.B.W., A.B.; Project lead: J.W.L., F.E., F.d.B., A.B.; EM Protocol development: J.B.W., M.P., R.L.S.; EM sample preparation and imaging: J.B.W.; Development of EM image quality assessment tools: Y.W.; Electroporations : S.R.; Area photoactivations: S.R., A.B.; X-ray imaging and analysis: J.B.W.; Sample sectioning: R.L.S.; EM images stitching and coarse elastic alignment: Y.W.; Two-photon imaging and analysis: J.B.W., A.B., F.K., K.N.K.; 2P to EM image registration: J.B.W., A.B.; Neuronal tracing: J.B.W., J.H.S.; Connectome analysis: J.B.W.; Single-cell photoactivations: F.K.; Datasets synchronization: F.K.; Development and testing of LDA-based classifier: F.K., J.B.W., G.F.P.S.; Cross-modality prediction of functional morphotypes: F.K.; Rendering of neuronal morphologies: J.B.W., F.K.; Cross-modality neuronal morphology registration: A.B. Modeling: A.B.; HCR FISH: F.K., H.N.; Atlas management: S.V., D.B.; NBLAST quantification: M.E., F.K., S.V.; H2B-GCaMP7f transgenic line generation: I.H.B.; cyto-GCaMP8s transgenic line generation: H.N.; Funding acquisition: J.W.L., F.E., F.d.B., D.B., A.B. Conceptualization of figures: J.B.W., F.K., G.F.P.S., A.B.; Writing of manuscript: J.B.W., A.B.; Correspondence and requests for materials should be addressed to J.B.W. and A.B.

Acknowledgments

We thank Zetta AI for alignment, cell segmentation, synapse detection & assignment, and hosting CAVE. We are grateful to Thomas Macrina for his assistance with connectome analysis, Paul Teufel for his initial help with segmentation, Zachary Miller for his contributions to manual registration, and Hillary Jean-Gilles for her help with tracing.

Bibliography

Akerman, C.J. and Cline, H.T. (2006) ‘Depolarizing GABAergic Conductances Regulate the Balance of Excitation to Inhibition in the Developing Retinotectal Circuit *In Vivo*’, *The Journal of Neuroscience*, 26(19), pp. 5117–5130. Available at: https://doi.org/10.1523/JNEUROSCI.0319-

06.2006.

Ammer, G. *et al.* (2023) 'Multilevel visual motion opponency in Drosophila', *Nature Neuroscience*, pp. 1–12. Available at: https://doi.org/10.1038/s41593-023-01443-z.

Arshadi, C. *et al.* (2021) 'SNT: a unifying toolbox for quantification of neuronal anatomy', *Nature Methods*, 18(4), pp. 374–377. Available at: https://doi.org/10.1038/s41592-021-01105-7.

Avants, B.B., Tustison, N. and Johnson, H. (2015) 'Advanced Normalization Tools (ANTS)'.

Bae, J.A. *et al.* (2018) 'Digital Museum of Retinal Ganglion Cells with Dense Anatomy and Physiology', *Cell*, 173(5), pp. 1293-1306.e19. Available at: https://doi.org/10.1016/j.cell.2018.04.040.

Bahl, A. and Engert, F. (2020) 'Neural circuits for evidence accumulation and decision making in larval zebrafish', *Nature Neuroscience*, 23(1), pp. 94–102. Available at: https://doi.org/10.1038/s41593-019-0534-9.

Bargmann, C.I. and Marder, E. (2013) 'From the connectome to brain function.', *Nature methods*, 10(6), pp. 483–90.

Bates, A.S. *et al.* (2020) 'Complete Connectomic Reconstruction of Olfactory Projection Neurons in the Fly Brain', *Current Biology*, 30(16), pp. 3183-3199.e6. Available at: https://doi.org/10.1016/j.cub.2020.06.042.

Bianco, I.H. *et al.* (2012) 'The Tangential Nucleus Controls a Gravito-inertial Vestibulo-ocular Reflex', *Current Biology*, 22(14), pp. 1285–1295. Available at: https://doi.org/10.1016/j.cub.2012.05.026.

Bogovic, J.A. *et al.* (2016) 'Robust registration of calcium images by learned contrast synthesis', in *2016 IEEE 13th International Symposium on Biomedical Imaging (ISBI)*. *2016 IEEE 13th International Symposium on Biomedical Imaging (ISBI 2016)*, Prague, Czech Republic: IEEE, pp. 1123–1126. Available at: https://doi.org/10.1109/ISBI.2016.7493463.

Boulanger-Weill, J. *et al.* (2017) 'Functional Interactions between Newborn and Mature Neurons Leading to Integration into Established Neuronal Circuits', *Current Biology*, 27(12), pp. 1707-1720.e5. Available at: https://doi.org/10.1016/j.cub.2017.05.029.

Briggman, K.L., Helmstaedter, M. and Denk, W. (2011) 'Wiring specificity in the direction-selectivity circuit of the retina', *Nature*, 471(7337), pp. 183–188. Available at: https://doi.org/10.1038/nature09818.

Brody, C.D. and Hanks, T.D. (2016) 'Neural underpinnings of the evidence accumulator', *Current Opinion in Neurobiology*, 37, pp. 149–157. Available at: https://doi.org/10.1016/j.conb.2016.01.003.

Chen, X. *et al.* (2018) 'Brain-wide Organization of Neuronal Activity and Convergent Sensorimotor Transformations in Larval Zebrafish', *Neuron*, 100(4), pp. 876-890.e5. Available at: https://doi.org/10.1016/j.neuron.2018.09.042.

Choi, H.M.T. *et al.* (2018) 'Third-generation *in situ* hybridization chain reaction: multiplexed, quantitative, sensitive, versatile, robust', *Development*, 145(12), p. dev165753. Available at: https://doi.org/10.1242/dev.165753.

Choi, K., Kim, W.K. and Hyeon, C. (2023) 'Polymer Physics-Based Classification of Neurons', *Neuroinformatics*, 21(1), pp. 177–193. Available at: https://doi.org/10.1007/s12021-022-09605-3.

Costa, M. *et al.* (2016) 'NBLAST: Rapid, Sensitive Comparison of Neuronal Structure and Construction of Neuron Family Databases', *Neuron*, 91(2), pp. 293–311. Available at:

https://doi.org/10.1016/j.neuron.2016.06.012.

Dana, H. *et al.* (2019) ‘High-performance calcium sensors for imaging activity in neuronal populations and microcompartments’, *Nature Methods*, 16(7), pp. 649–657. Available at: https://doi.org/10.1038/s41592-019-0435-6.

Ding, Z. *et al.* (2023) ‘Functional connectomics reveals general wiring rule in mouse visual cortex’. Available at: https://doi.org/10.1101/2023.03.13.531369.

Dombrovski, M. *et al.* (2023) ‘Synaptic gradients transform object location to action’, *Nature*, 613(7944), pp. 534–542. Available at: https://doi.org/10.1038/s41586-022-05562-8.

Dorkenwald, S. *et al.* (2023) ‘CAVE: Connectome Annotation Versioning Engine’. Available at: https://doi.org/10.1101/2023.07.26.550598.

Dorkenwald, S. *et al.* (2024) ‘Neuronal wiring diagram of an adult brain’, *Nature*, 634(8032), pp. 124–138. Available at: https://doi.org/10.1038/s41586-024-07558-y.

Dowell, C.K. *et al.* (2024) ‘Kinematically distinct saccades are used in a context-dependent manner by larval zebrafish’, *Current Biology*, 34(19), pp. 4382-4396.e5. Available at: https://doi.org/10.1016/j.cub.2024.08.008.

Dragomir, E.I., Štih, V. and Portugues, R. (2020) ‘Evidence accumulation during a sensorimotor decision task revealed by whole-brain imaging’, *Nature Neuroscience*, 23(1), pp. 85–93. Available at: https://doi.org/10.1038/s41593-019-0535-8.

Feng, L., Zhao, T. and Kim, J. (2015) ‘neuTube 1.0: A New Design for Efficient Neuron Reconstruction Software Based on the SWC Format’, *eneuro*, 2(1), p. ENEURO.0049-14.2014. Available at: https://doi.org/10.1523/ENEURO.0049-14.2014.

Filippi, A., Mueller, T. and Driever, W. (2014) ‘vglut2 and gad expression reveal distinct patterns of dual GABAergic versus glutamatergic cotransmitter phenotypes of dopaminergic and noradrenergic neurons in the zebrafish brain’, *Journal of Comparative Neurology*, 522(9), pp. 2019–2037. Available at: https://doi.org/10.1002/cne.23524.

Förster, D. *et al.* (2018) ‘Optogenetic precision toolkit to reveal form, function and connectivity of single neurons’, *Methods*, 150, pp. 42–48. Available at: https://doi.org/10.1016/j.ymeth.2018.08.012.

Freeman, J. *et al.* (2014) ‘Mapping brain activity at scale with cluster computing’, *Nature Methods*, 11(9), pp. 941–950. Available at: https://doi.org/10.1038/nmeth.3041.

Friedrich, R.W. and Wanner, A.A. (2021) ‘Dense Circuit Reconstruction to Understand Neuronal Computation: Focus on Zebrafish’, *Annual Review of Neuroscience*, 44, pp. 275–293. Available at: https://doi.org/10.1146/annurev-neuro-110220-013050.

Fujita, M. *et al.* (2011) ‘Assembly and patterning of the vascular network of the vertebrate hindbrain’, *Development*, 138(9), pp. 1705–1715. Available at: https://doi.org/10.1242/dev.058776.

Groschner, L.N. *et al.* (2018) ‘Dendritic Integration of Sensory Evidence in Perceptual Decision-Making’, *Cell*, 173(4), pp. 894-905.e13. Available at: https://doi.org/10.1016/j.cell.2018.03.075.

Han, X. *et al.* (2023) ‘Whole human-brain mapping of single cortical neurons for profiling morphological diversity and stereotypy’, *SCIENCE ADVANCES* [Preprint].

Hanks, T.D. *et al.* (2015) ‘Distinct relationships of parietal and prefrontal cortices to evidence accumulation’, *Nature*, 520(7546), pp. 220–223. Available at: https://doi.org/10.1038/nature14066.

Hanks, T.D. and Summerfield, C. (2017) ‘Perceptual Decision Making in Rodents, Monkeys, and

1105 Humans', *Neuron*, 93(1), pp. 15–31. Available at: https://doi.org/10.1016/j.neuron.2016.12.003.

1106 Hayworth, K.J. *et al.* (2014) 'Imaging ATUM ultrathin section libraries with WaferMapper: a multi-
1107 scale approach to EM reconstruction of neural circuits', *Frontiers in Neural Circuits*, 8. Available at:
1108 https://doi.org/10.3389/fncir.2014.00068.

1109 Higashijima, S.-I., Mandel, G. and Fetcho, J.R. (2004) 'Distribution of prospective glutamatergic,
1110 glycinergic, and GABAergic neurons in embryonic and larval zebrafish', *The Journal of Comparative*
1111 *Neurology*, 480(1), pp. 1–18. Available at: https://doi.org/10.1002/cne.20278.

1112 Hildebrand, D.G.C. *et al.* (2017) 'Whole-brain serial-section electron microscopy in larval zebrafish',
1113 *Nature* [Preprint]. Available at: https://doi.org/10.1038/nature22356.

1114 Holler, S. *et al.* (2021) 'Structure and function of a neocortical synapse', *Nature*, 591(7848), pp.
1115 111–116. Available at: https://doi.org/10.1038/s41586-020-03134-2.

1116 Hua, Y., Laserstein, P. and Helmstaedter, M. (2015) 'Large-volume en-bloc staining for electron
1117 microscopy-based connectomics', *Nature Communications*, 6(1), p. 7923. Available at:
1118 https://doi.org/10.1038/ncomms8923.

1119 Joy, D.C. (2002) 'SMART BlackwellScience,Ltd – a program to measure SEM resolution and
1120 imaging performance', *Journal of Microscopy* [Preprint].

1121 Katz, L.N. *et al.* (2016) 'Dissociated functional significance of decision-related activity in the primate
1122 dorsal stream', *Nature*, 535(7611), pp. 285–288. Available at: https://doi.org/10.1038/nature18617.

1123 Khona, M. and Fiete, I.R. (2022) 'Attractor and integrator networks in the brain', *Nature Reviews*
1124 *Neuroscience*, 23(12), pp. 744–766. Available at: https://doi.org/10.1038/s41583-022-00642-0.

1125 Kramer, A. *et al.* (2019) 'Neuronal architecture of a visual center that processes optic flow', *Neuron*,
1126 103(1), pp. 118-132.e7. Available at: https://doi.org/10.1016/j.neuron.2019.04.018.

1127 Kubo, F. *et al.* (2014) 'Functional Architecture of an Optic Flow-Responsive Area that Drives
1128 Horizontal Eye Movements in Zebrafish', *Neuron*, 81(6), pp. 1344–1359. Available at:
1129 https://doi.org/10.1016/j.neuron.2014.02.043.

1130 Kunst, M. *et al.* (2019) 'A Cellular-Resolution Atlas of the Larval Zebrafish Brain', *Neuron*, 103(1),
1131 pp. 21-38.e5. Available at: https://doi.org/10.1016/j.neuron.2019.04.034.

1132 Lanciego, J.L., Luquin, N. and Obeso, J.A. (2012) 'Functional Neuroanatomy of the Basal Ganglia',
1133 *Cold Spring Harbor Perspectives in Medicine*, 2(12), pp. a009621–a009621. Available at:
1134 https://doi.org/10.1101/cshperspect.a009621.

1135 Lappalainen, J.K. *et al.* (2024) 'Connectome-constrained networks predict neural activity across the
1136 fly visual system', *Nature*, pp. 1–9. Available at: https://doi.org/10.1038/s41586-024-07939-3.

1137 Lee, W.-C.A. *et al.* (2016) 'Anatomy and function of an excitatory network in the visual cortex',
1138 *Nature*, 532(7599), pp. 370–374. Available at: https://doi.org/10.1038/nature17192.

1139 Li, Y. *et al.* (2017) 'Metrics for comparing neuronal tree shapes based on persistent homology',
1140 *PLOS ONE*, 12(8), p. e0182184. Available at: https://doi.org/10.1371/journal.pone.0182184.

1141 Lister, J.A. *et al.* (1999) 'nacre encodes a zebrafish microphthalmia-related protein that regulates
1142 neural-crest-derived pigment cell fate', *Development*, 126(17), pp. 3757–3767. Available at:
1143 https://doi.org/10.1242/dev.126.17.3757.

1144 Macrina, T. *et al.* (2021) 'Petascale neural circuit reconstruction: automated methods'. Available at:
1145 https://doi.org/10.1101/2021.08.04.455162.

1146 Naumann, E.A. *et al.* (2016) 'From Whole-Brain Data to Functional Circuit Models: The Zebrafish
1147 Optomotor Response', *Cell*, 167(4), pp. 947-960.e20. Available at:
1148 https://doi.org/10.1016/j.cell.2016.10.019.

1149 Newsome, W.T., Britten, K.H. and Movshon, J.A. (1989) 'Neuronal correlates of a perceptual
1150 decision', *Nature*, 341(6237), pp. 52–54. Available at: https://doi.org/10.1038/341052a0.

1151 Orger, M.B. *et al.* (2008) 'Control of visually guided behavior by distinct populations of spinal
1152 projection neurons', *Nature Neuroscience*, 11(3), pp. 327–333. Available at:
1153 https://doi.org/10.1038/nn2048.

1154 Pallotto, M. *et al.* (2015) 'Extracellular space preservation aids the connectomic analysis of neural
1155 circuits', *eLife*, 4, p. e08206. Available at: https://doi.org/10.7554/eLife.08206.

1156 Patterson, G.H. and Lippincott-Schwartz, J. (2002) 'A Photoactivatable GFP for Selective
1157 Photolabeling of Proteins and Cells', *Science*, 297(5588), pp. 1873–1877. Available at:
1158 https://doi.org/10.1126/science.1074952.

1159 Peloggia, J. *et al.* (2024) 'Paired and solitary ionocytes in the zebrafish olfactory epithelium'.
1160 Available at: https://doi.org/10.1101/2024.11.08.620918.

1161 Petkova, M.D. (2020) 'Correlative Light and Electron Microscopy in an Intact Larval Zebrafish'.

1162 Petrucco, L. *et al.* (2023) 'Neural dynamics and architecture of the heading direction circuit in
1163 zebrafish', *Nature Neuroscience*, pp. 1–9. Available at: https://doi.org/10.1038/s41593-023-01308-5.

1164 Pnevmatikakis, E.A. and Giovannucci, A. (2017) 'NoRMCorre: An online algorithm for piecewise
1165 rigid motion correction of calcium imaging data', *Journal of Neuroscience Methods*, 291, pp. 83–94.
1166 Available at: https://doi.org/10.1016/j.jneumeth.2017.07.031.

1167 Popovych, S. *et al.* (2024) 'Petascale pipeline for precise alignment of images from serial section
1168 electron microscopy', *Nature Communications*, 15(1), p. 289. Available at:
1169 https://doi.org/10.1038/s41467-023-44354-0.

1170 Randlett, O., Wee, C.L., Naumann, E.A., *et al.* (2015) 'Whole-brain activity mapping onto a zebrafish
1171 brain atlas', *Nature Methods*, 12(11), pp. 1039–1046. Available at:
1172 https://doi.org/10.1038/nmeth.3581.

1173 Randlett, O., Wee, C.L., Naumann, E. a, *et al.* (2015) 'Whole-brain activity mapping onto a zebrafish
1174 brain atlas', *Nature Methods*, 12(September), pp. 1–12. Available at:
1175 https://doi.org/10.1038/nmeth.3581.

1176 Sato, M. *et al.* (2000) 'TEASAR: tree-structure extraction algorithm for accurate and robust
1177 skeletons', in *Proceedings the Eighth Pacific Conference on Computer Graphics and Applications*.
1178 *the Eighth Pacific Conference on Computer Graphics and Applications*, Hong Kong, China: IEEE
1179 Comput. Soc, pp. 281–449. Available at: https://doi.org/10.1109/PCCGA.2000.883951.

1180 Satou, C. *et al.* (2013) 'Transgenic tools to characterize neuronal properties of discrete populations
1181 of zebrafish neurons', *Development*, 140(18), pp. 3927–3931. Available at:
1182 https://doi.org/10.1242/dev.099531.

1183 Schindelin, J. *et al.* (2012) 'Fiji: an open-source platform for biological-image analysis', *Nature*
1184 *Methods*, 9(7), pp. 676–682. Available at: https://doi.org/10.1038/nmeth.2019.

1185 Schlegel, P. *et al.* (2021) 'Information flow, cell types and stereotypy in a full olfactory connectome',
1186 *eLife*, 10, p. e66018. Available at: https://doi.org/10.7554/eLife.66018.

1187 Schlegel, P. *et al.* (2024) 'Whole-brain annotation and multi-connectome cell typing of Drosophila',

Nature, 634(8032), pp. 139–152. Available at: https://doi.org/10.1038/s41586-024-07686-5.

Schlegel, P. *et al.* (2025) 'navis-org/navis: Version 1.10.0'. Zenodo. Available at: https://doi.org/10.5281/zenodo.14827782.

Seung, H.S. (1996) 'How the brain keeps the eyes still', *Proceedings of the National Academy of Sciences*, 93(23), pp. 13339–13344. Available at: https://doi.org/10.1073/pnas.93.23.13339.

Stringer, C., & Pachitariu, M. (2025). Cellpose3: One-click image restoration for improved cellular segmentation. Nature Methods, 22(3), 592–599. https://doi.org/10.1038/s41592-025-02595-5

Shainer, I. *et al.* (2023) 'A single-cell resolution gene expression atlas of the larval zebrafish brain', *Science Advances*, 9(eade9909). Available at: https://doi.org/10.1126/sciadv.ade9909.

Shainer, I. *et al.* (2025) 'Transcriptomic neuron types vary topographically in function and morphology', *Nature*, 638(8052), pp. 1023–1033. Available at: https://doi.org/10.1038/s41586-024-08518-2.

Shapson-Coe, A. *et al.* (2024) 'A petavoxel fragment of human cerebral cortex reconstructed at nanoscale resolution', *Science*, 384(6696), p. eadk4858. Available at: https://doi.org/10.1126/science.adk4858.

Shiu, P.K. *et al.* (2024) 'A Drosophila computational brain model reveals sensorimotor processing', *Nature*, 634(8032), pp. 210–219. Available at: https://doi.org/10.1038/s41586-024-07763-9.

Silberberg, G., Gupta, A. and Markram, H. (2002) 'Stereotypy in neocortical microcircuits', *Trends in Neurosciences*, 25(5), pp. 227–230. Available at: https://doi.org/10.1016/S0166-2236(02)02151-3.

Silversmith, W. *et al.* (2022) 'Igneous: Distributed dense 3D segmentation meshing, neuron skeletonization, and hierarchical downsampling', *Frontiers in Neural Circuits*, 16, p. 977700. Available at: https://doi.org/10.3389/fncir.2022.977700.

Svara, F. *et al.* (2022) 'Automated synapse-level reconstruction of neural circuits in the larval zebrafish brain', *Nature Methods*, 19(11), pp. 1357–1366. Available at: https://doi.org/10.1038/s41592-022-01621-0.

Tapia, J.C. *et al.* (2012) 'High-contrast en bloc staining of neuronal tissue for field emission scanning electron microscopy', *Nature Protocols*, 7(2), pp. 193–206. Available at: https://doi.org/10.1038/nprot.2011.439.

The MICrONS Consortium *et al.* (2021) 'Functional connectomics spanning multiple areas of mouse visual cortex'. Available at: https://doi.org/10.1101/2021.07.28.454025.

Turner, N.L. *et al.* (2022) 'Reconstruction of neocortex: Organelles, compartments, cells, circuits, and activity', *Cell*, 185(6), pp. 1082-1100.e24. Available at: https://doi.org/10.1016/j.cell.2022.01.023.

Turner-Evans, D.B. *et al.* (2020) 'The Neuroanatomical Ultrastructure and Function of a Biological Ring Attractor', *Neuron*, 108(1), pp. 145-163.e10. Available at: https://doi.org/10.1016/j.neuron.2020.08.006.

Umargono, E., Suseno, J.E. and S. K., V.G. (2019) 'K-Means Clustering Optimization using the Elbow Method and Early Centroid Determination Based-on Mean and Median':, in *Proceedings of the International Conferences on Information System and Technology*. *International Conferences on Information System and Technology*, Yogyakarta, Indonesia: SCITEPRESS - Science and Technology Publications, pp. 234–240. Available at: https://doi.org/10.5220/0009908402340240.

Vishwanathan, A. *et al.* (2017) 'Electron Microscopic Reconstruction of Functionally Identified Cells

in a Neural Integrator', *Current Biology*, 27(14), pp. 2137-2147.e3. Available at: https://doi.org/10.1016/j.cub.2017.06.028.

Vishwanathan, A. *et al.* (2024) 'Predicting modular functions and neural coding of behavior from a synaptic wiring diagram', *Nature Neuroscience*, pp. 1–12. Available at: https://doi.org/10.1038/s41593-024-01784-3.

Wang, K. *et al.* (2019) 'Selective processing of all rotational and translational optic flow directions in the zebrafish pretectum and tectum', *BMC Biology*, 17(1), p. 29. Available at: https://doi.org/10.1186/s12915-019-0648-2.

Wanner, A.A. and Friedrich, R.W. (2020) 'Whitening of odor representations by the wiring diagram of the olfactory bulb', *Nature Neuroscience*, 23(3), pp. 433–442. Available at: https://doi.org/10.1038/s41593-019-0576-z.

Weigert, M. *et al.* (2018) 'Content-aware image restoration: pushing the limits of fluorescence microscopy', *Nature Methods*, 15(12), pp. 1090–1097. Available at: https://doi.org/10.1038/s41592-018-0216-7.

Weigert, M. *et al.* (2020) 'Star-convex Polyhedra for 3D Object Detection and Segmentation in Microscopy', in *2020 IEEE Winter Conference on Applications of Computer Vision (WACV)*. *2020 IEEE Winter Conference on Applications of Computer Vision (WACV)*, Snowmass Village, CO, USA: IEEE, pp. 3655–3662. Available at: https://doi.org/10.1109/WACV45572.2020.9093435.

Weigert, M. and Schmidt, U. (2022) 'Nuclei Instance Segmentation and Classification in Histopathology Images with Stardist', in *2022 IEEE International Symposium on Biomedical Imaging Challenges (ISBIC)*. *2022 IEEE International Symposium on Biomedical Imaging Challenges (ISBIC)*, Kolkata, India: IEEE, pp. 1–4. Available at: https://doi.org/10.1109/ISBIC56247.2022.9854534.

Witvliet, D. *et al.* (2021) 'Connectomes across development reveal principles of brain maturation', *Nature*, 596(7871), pp. 257–261. Available at: https://doi.org/10.1038/s41586-021-03778-8.

Wolf, S. *et al.* (2017) 'Sensorimotor computation underlying phototaxis in zebrafish', *Nature Communications*, 8(1), p. 651. Available at: https://doi.org/10.1038/s41467-017-00310-3.

Yang, R. *et al.* (2023) 'Cyclic structure with cellular precision in a vertebrate sensorimotor neural circuit', *Current Biology*, 33(11), pp. 2340-2349.e3. Available at: https://doi.org/10.1016/j.cub.2023.05.010.

Zhang, Y. *et al.* (2023) 'Fast and sensitive GCaMP calcium indicators for imaging neural populations', *Nature*, 615(7954), pp. 884–891. Available at: https://doi.org/10.1038/s41586-023-05828-9.

Zou, M., Friedrich, R.W. and Bianco, I.H. (2016) 'Targeted Electroporation in Embryonic, Larval, and Adult Zebrafish', in K. Kawakami, E.E. Patton, and M. Orger (eds) *Zebrafish: Methods and Protocols*. New York, NY: Springer New York, pp. 259–269. Available at: https://doi.org/10.1007/978-1-4939-3771-4_17.

Extended Data

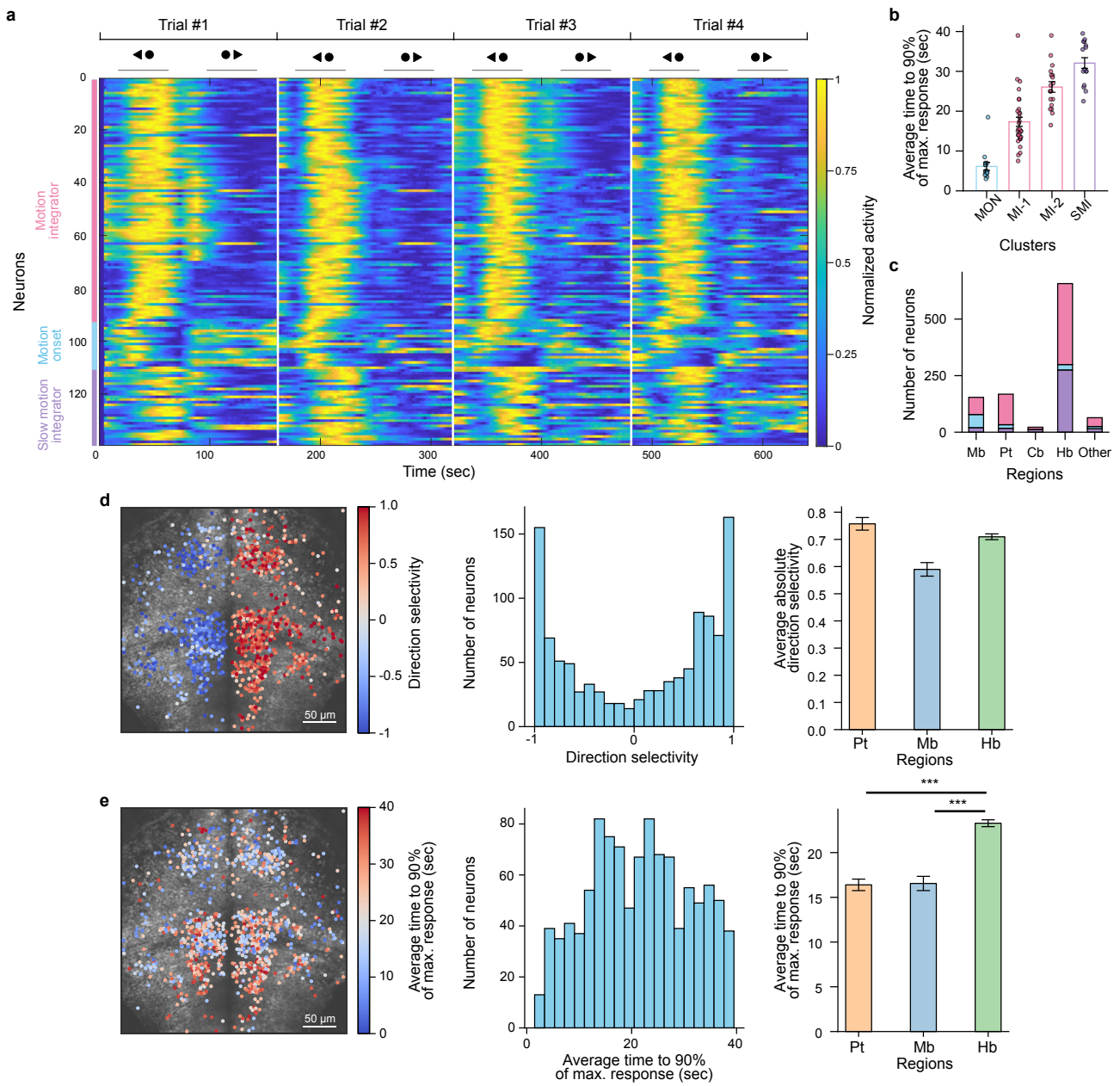

Extended Data Fig. 1 | Detailed analysis of neuronal functional recordings. (a) Raster plot of representative examples of direction-selective neurons belonging to the three functional classes. Four example trials, both for left- and rightward moving dots. Upper arrows represent the direction of motion and gray bars represent the stimulation epochs. Neurons are organized according to their functional responses (see left colored bars). Individual trials are separated by horizontal white bars. **(b)** Rise time to reach 90% of the maximal response for each k-means cluster. Each dot represents a single neuron. MON, motion onset neurons; MI-1, fast motion integrators; MI-2, intermediate motion integrators; SMI, slow motion integrators. **(c)** Distribution of neurons across brain regions and cluster types. (**d**) Left: spatial distribution of direction selectivity values for the three functional classes. Middle: histogram of direction selectivity values for the same population. Right: average values for neurons grouped by brain region. *** indicates $p < 0.001$ (two-sided t-test), (**e**) Same as (**d**) but for representing the time to reach 90% of the maximal response. Mb, midbrain; Pt, pretectum; Cb, cerebellum; Hb, hindbrain; Oth, other regions.

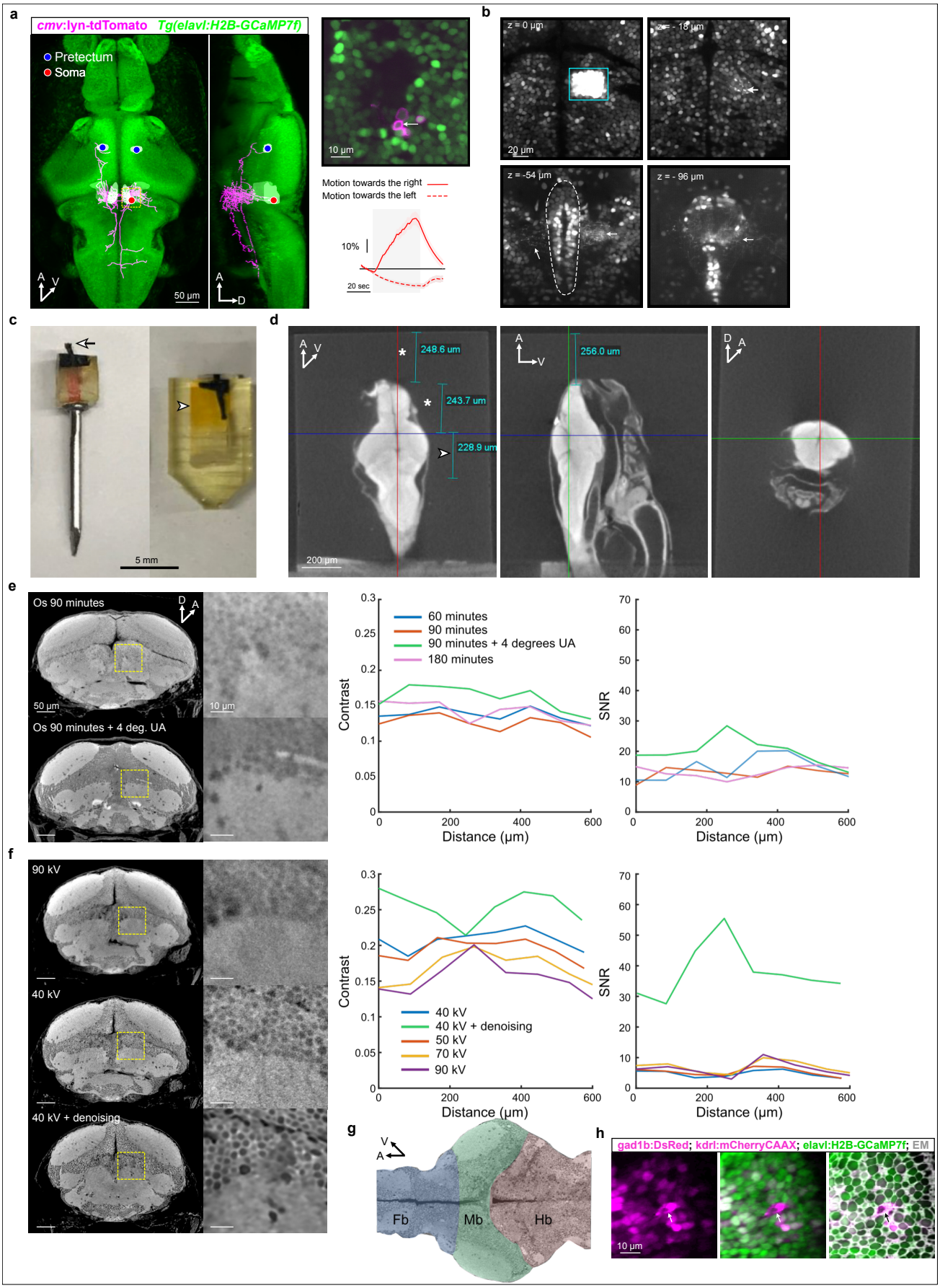

Extended Data Fig. 2 | Sample preparation and region of interest identification. (a) hindbrain sparse electroporations. Left panels: reconstructed neurons registered to a reference brain indicating soma and Pt locations. Note the projection pattern of the cells towards the Pt and ipsilateral and contralateral anterior hindbrain. The dashed yellow square is magnified in the top-right snippet. Right panels: two-photon single-plane image showing the somas of the electroporated neurons

together with response dynamics to rightward and leftward moving dots for one neuron (indicated by the white arrow). The activity responses are reminiscent of an evidence integrator. Activity traces show the average responses for 4 trials (SEM indicated by the red shaded area). Stimulation epoch is denoted by the shaded gray area. (**b**) Photoactivation of a group of neurons in the anterior hindbrain in *Tg(elavl3:H2B-GCaMP6s, gad1b:loxP-DsRed-loxP-GFP, alpha-tub:c3pa-GFP)* (cyan square). Cells project ventrally, ipsilaterally, and contralaterally close to the raphe (dashed outline at z=-54 µm from the photoactivation plane). Neuronal projections are indicated by the white arrows. **(c)** Left: A resin-embedded larva with the cast around the head trimmed (white arrow) for enhanced X-ray penetration. Right. Another larva re-embedded in resin after X-ray tomography before ultramicrotome sectioning. The limit between the two resin casts is denoted by the arrowhead. **(d)** Orthogonal X-ray tomography views of the main larva used in this study. The first panel shows the edges of the region of interest determined before the sections collection. By performing direct measurements using the X-ray microscope software we precisely targeted the sections collection by trimming away the unnecessary resin and tissue (white asterisks), keeping only the region of interest (white arrowhead) containing the anterior hindbrain and most of the identified neuronal projections (**a,b**). **(e)** First step of contrast and signal to noise ratio (SNR) improvement achieved by varying the Osmium (Os) incubation duration and incubating the Uranyl Acetate (UA) at 4°C instead of room temperature. Left panels: Representative X-ray tomography cross sections along the main axis of the larva and high-resolution snippets (corresponding to dashed yellow squares). Right panels: Contrast and SNR computed along the main axis of the fish, see **Extended Data Fig. 2g**. Each line represents the average of two fish per condition. **(f)** Similar to (**i**) showing the improvement by changing the X-ray imaging power. Notice the dose-dependent improvement as the power is lowered from 90 to 40 kV. **(g)** Reference fish imaged with X-ray (dorsal section plane) indicating where the contrast and SNR measurements were performed. Distances correspond to the upper plots. Fb, forebrain; Mb, midbrain; Hb, hindbrain. **(h)** Images showing the alignment between the 2P and EM datasets confirming the precise correspondence of a blood vessel cross-section (indicated by a white arrow) across imaging modalities. Abbreviations: A, anterior; D, dorsal; V, ventral.

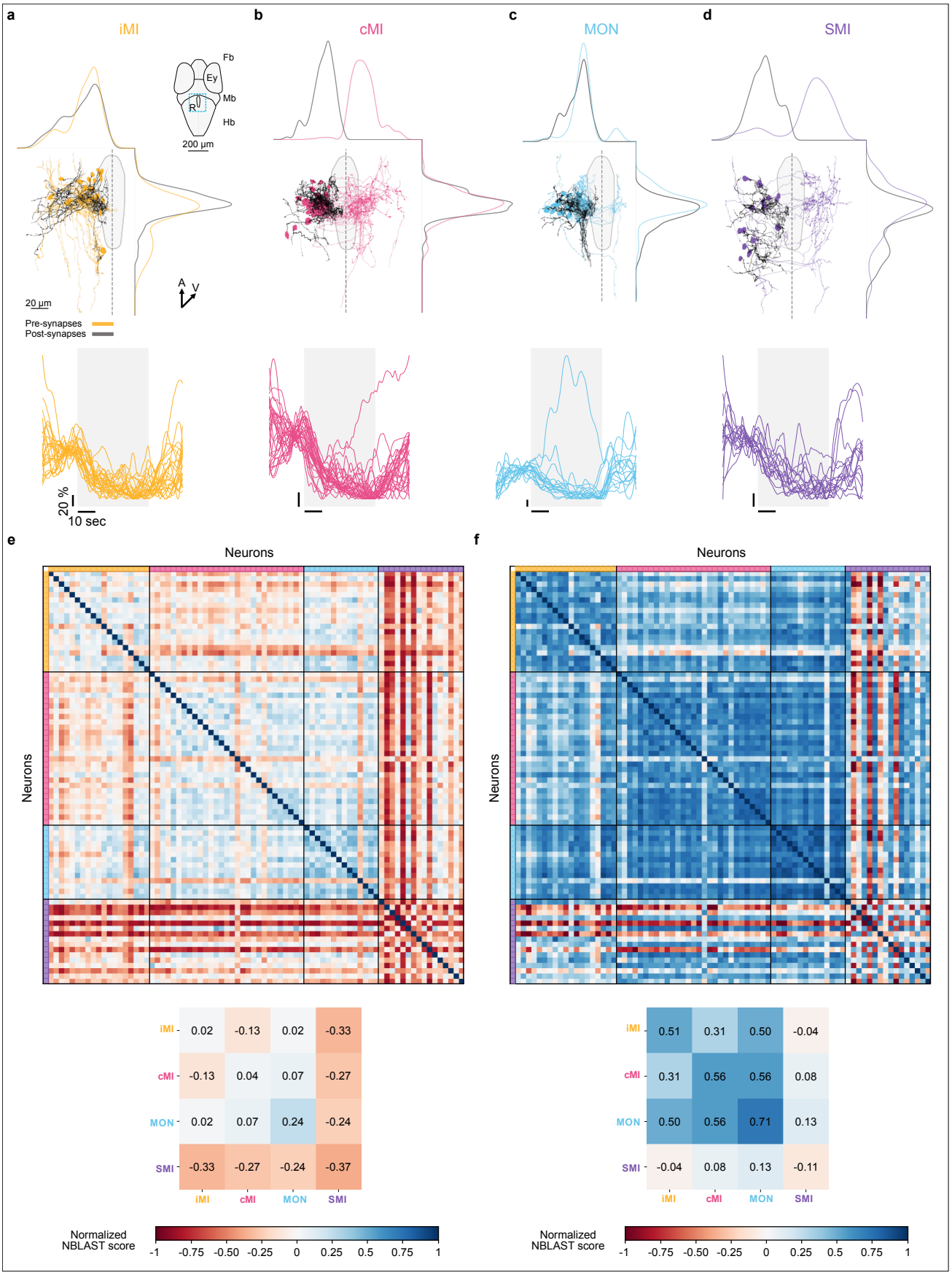

Extended Data Fig. 3 | Structure-function relationship and morphological diversity within and in-between clusters. **(a)** Structure-function relationship of functionally imaged and reconstructed iMI neurons as in **Fig. 1f-i** but in dorsal view. Somas and axons are colored in orange and dendrites in black. Dashed line represents the midline. Surrounding plots are distribution of presynaptic (orange) and postsynaptic (black) synapses along the x (top) and y (right) axes. Right: schematic showing coarse brain organization (dorsal-to-ventral view) and location of the reconstructed neurons below (blue dashed square) surrounding outlines of the raphe (also shown below). Right: traces representing the normalized ΔF/F0 neuronal

activity over time for motion in the opposite, null direction. (**b-d**) shows identical representation for other neuron types. All neurons are registered to a reference brain (Randlett, Wee, E. a Naumann, *et al.*, 2015). Abbreviations: Mb, midbrain; Hb, hindbrain; R, raphe; Ey, eye; A, anterior; V, ventral. (**e-f**) Top matrices: Normalized NBLAST matrix organized by functional types using morphological similarity distances computed using *Drosophila* neurons (**e**) and the functionally identified neurons in this study (**f**). Bottom : averaged NBLAST scores within and across functional types.

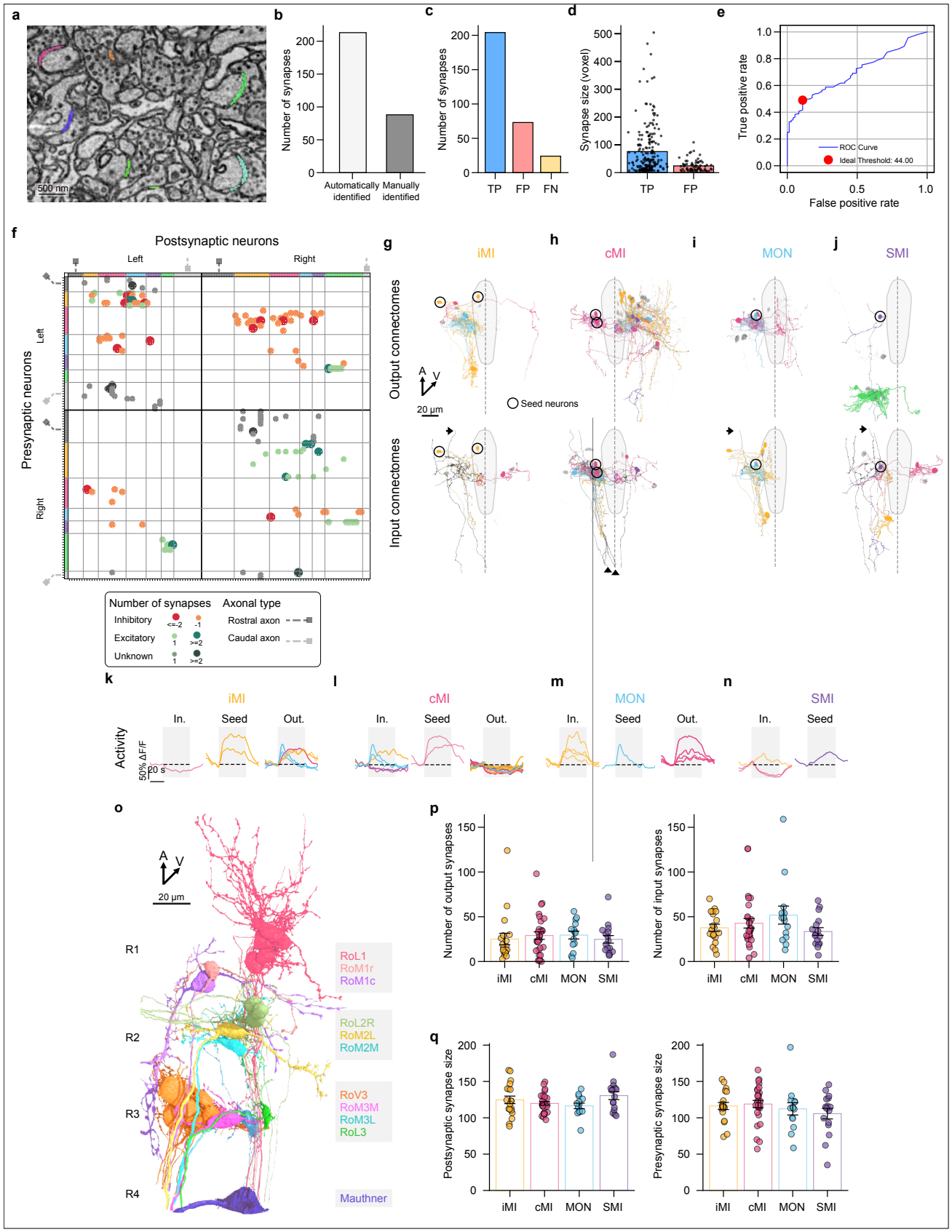

Extended Data Fig. 4 | Details of automated synapses predictions and functional dynamics of reconstructed connectomes examples. (a) Raw EM image with automatically detected synaptic clefts in color. (**b**) Histogram showing the number of automatically identified and manually identified synapses by visually inspecting two dendrites and one axon. (**c**) Classification of automatically predicted synapses as true positives, false positives (not synapses) and false negatives (missing synapses). (**d**) Comparison of synapse sizes between true positives and false positives. (**e**) Receiver Operating Characteristic (ROC) curve analysis establishing a size threshold at 44 voxels to exclude 90% of false positive synapses. (**f**) Connectivity matrix with neurons and connected axons sorted according to their functional types and hemispheres (thick black bars separate the left and right hemispheres). Rostral axons, truncated at the rostral end of the imaging volume, terminate within the volume, while caudal axons are truncated at the caudal end of the volume and also terminate within it. Axons that traverse the entire imaging volume are not shown. (**g-h**) Representative example connectomes (dorsal view) for one or two seed cells with corresponding activity related to **Fig. 2c-j.** All neuronal parts (some, axon and dendrites) are colored identically. All neurons are registered to a reference brain (Randlett, Wee, E. a Naumann, *et al.*, 2015). Black arrows and arrowheads represent example rostral and caudal axons, respectively. **(k-n)** Activity traces for the neurons shown in this figure **(g-j)** and **Fig. 2c-j** with visual stimulation epochs indicated by gray shaded areas. Dashes black lines correspond to $\Delta F/F=0$. **(o)** Rendering of identified reticulospinal neurons belonging to rhombomeres 1 to 4 (R1-4). (**p**) Histograms showing the distributions of synapses numbers and sizes (**q**) for each functionally identified cell type. Error bars represent standard error of the mean (SEM). Individual dots represent single neurons.

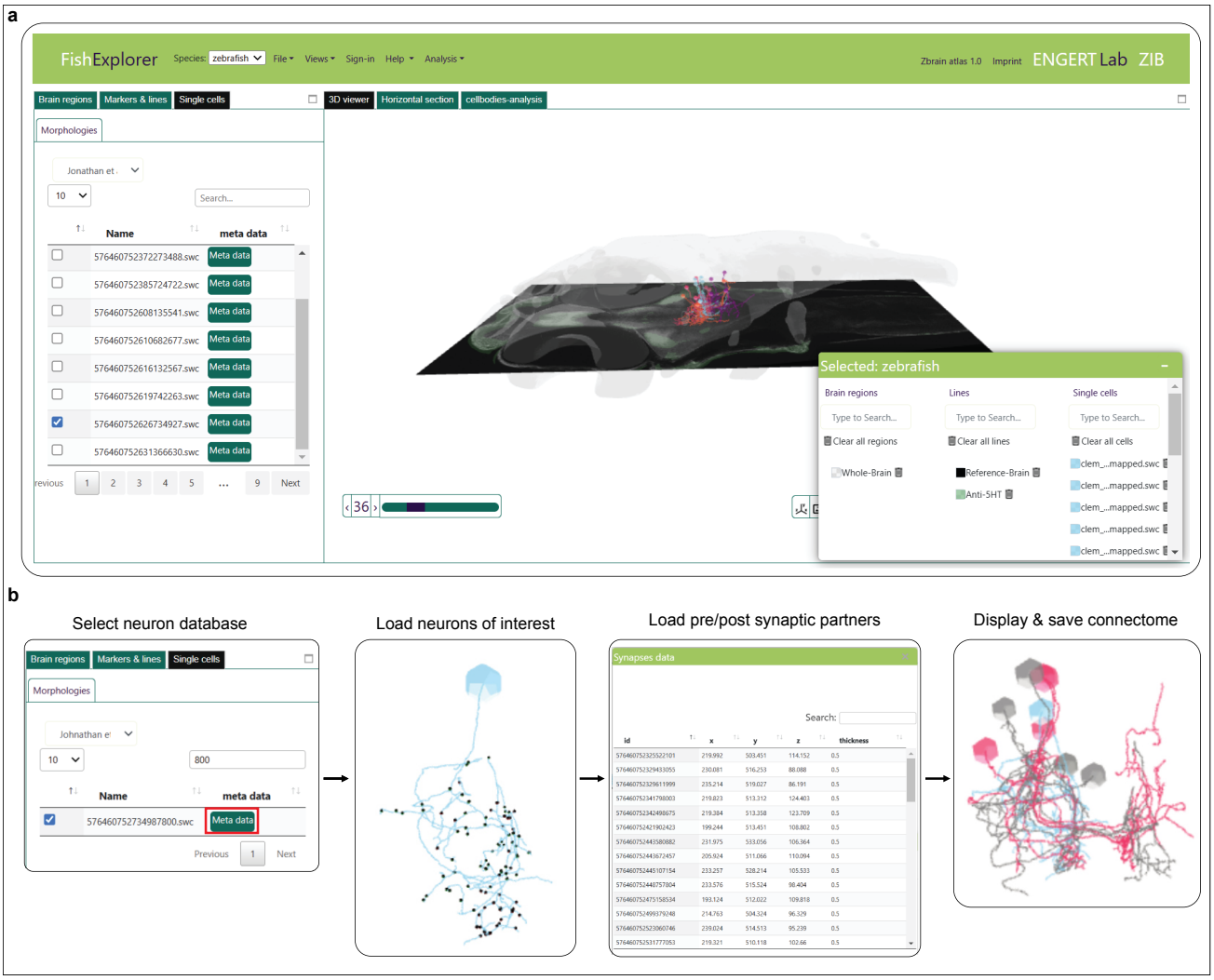

Extended Data Fig. 5 | Details of automated synapses prediction and online neurons and connectome visualization. **(a)** Multi-modal and multi species web based atlas platform contains annotations of all anatomical brain subdivisions and XX registered transgenic lines for deeper analyses. **(b)** Flowchart to visualize single neurons and connectomes in FishExplorer. To visualize single cells and connectomes users should first select the neuron of interest by selecting the appropriate dataset (correlated light and EM, photoactivated neurons, EM whole-brain Atlas) and tracer. To display the connectomes of a cell, users should then click the meta information button in the front of the neuron name highlighted by the red rectangle. The window shows meta information, input and out partners will appear on screen. Next, the user can load all the output partners by clicking the 'load all output' button. The researchers can also save and share their current analysis 'scene' of connectomes with the community.

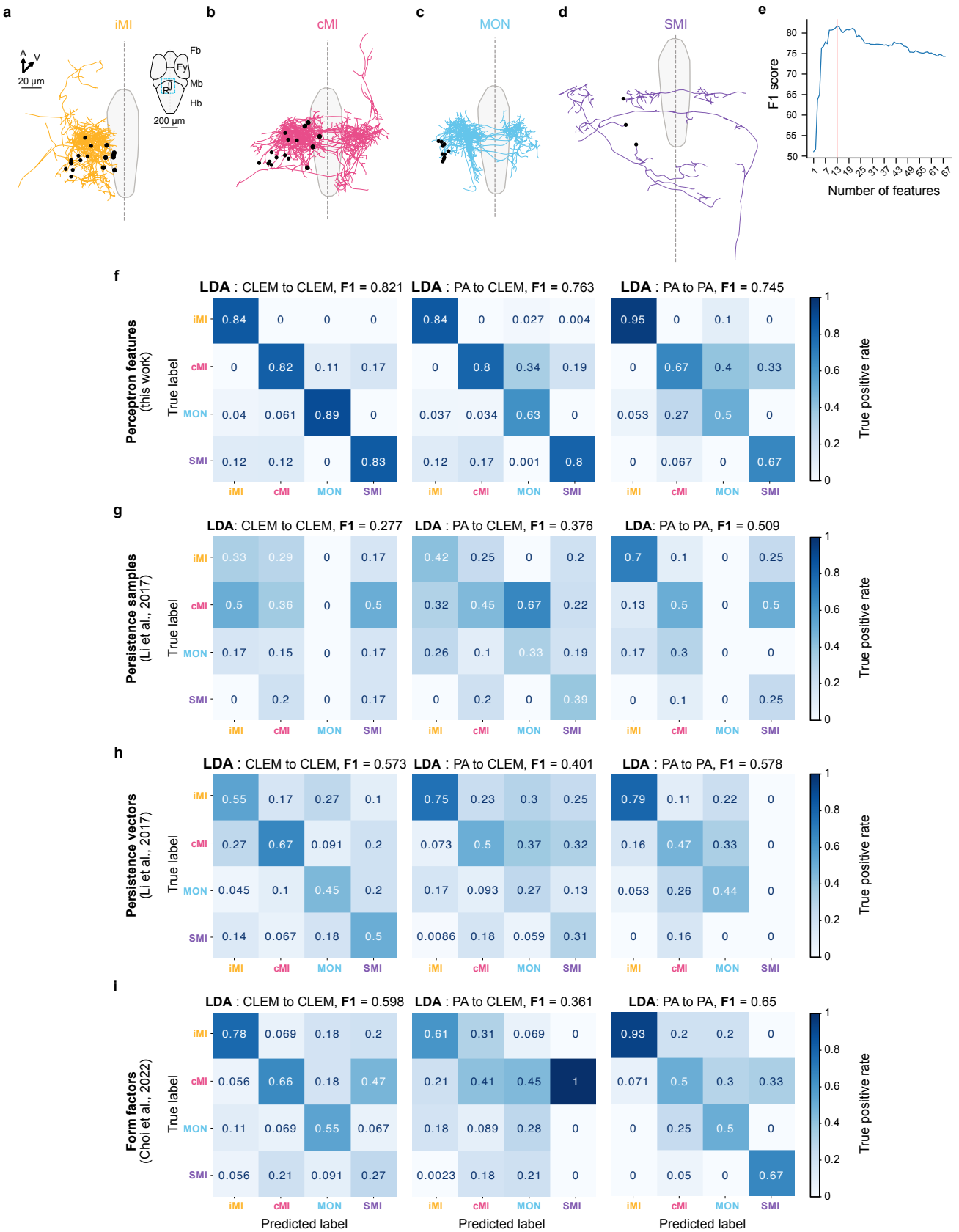

Extended Data Fig. 6 | Photoactivated neurons diversity and LDA benchmarking. (a) Structure-function relationship of functionally imaged and photoactivated neurons as in **Fig 3b-e** but in dorsal view. Right: schematic showing coarse brain organization (dorsal-to-ventral view) and location of the reconstructed neurons below (blue dashed square) surrounding outlines of the raphe (also shown below). (**b-d**) shows identical representation for other neuron types. All neurons are registered to a reference brain (Randlett, Wee, E. a Naumann, *et al.*, 2015). Abbreviations: Mb, midbrain; Hb, hindbrain; R, raphe; Ey, eye; A, anterior; V, ventral. (**e**) F1-score as a function of the feature subset size used for **Fig. 3g** and below. The red line represents the number of features (n=13) yielding the maximum F1 score. (**f**) Left, LDA confusion matrix of TPR using CLEM cells as the ground truth and predicting CLEM cells. F1 score for the entire matrix is indicated

in the title. Middle same as left but using PA as ground truth and predicting CLEM cells. Right, same as left but using PA as ground truth and predicting PA cells. LDA, linear discriminant analysis; RF, random forest. (**g-i**) Prediction of functional types using other established methods (persistence samples, persistence vectors and form factors metrics, respectively). Display is identical as (**f**).

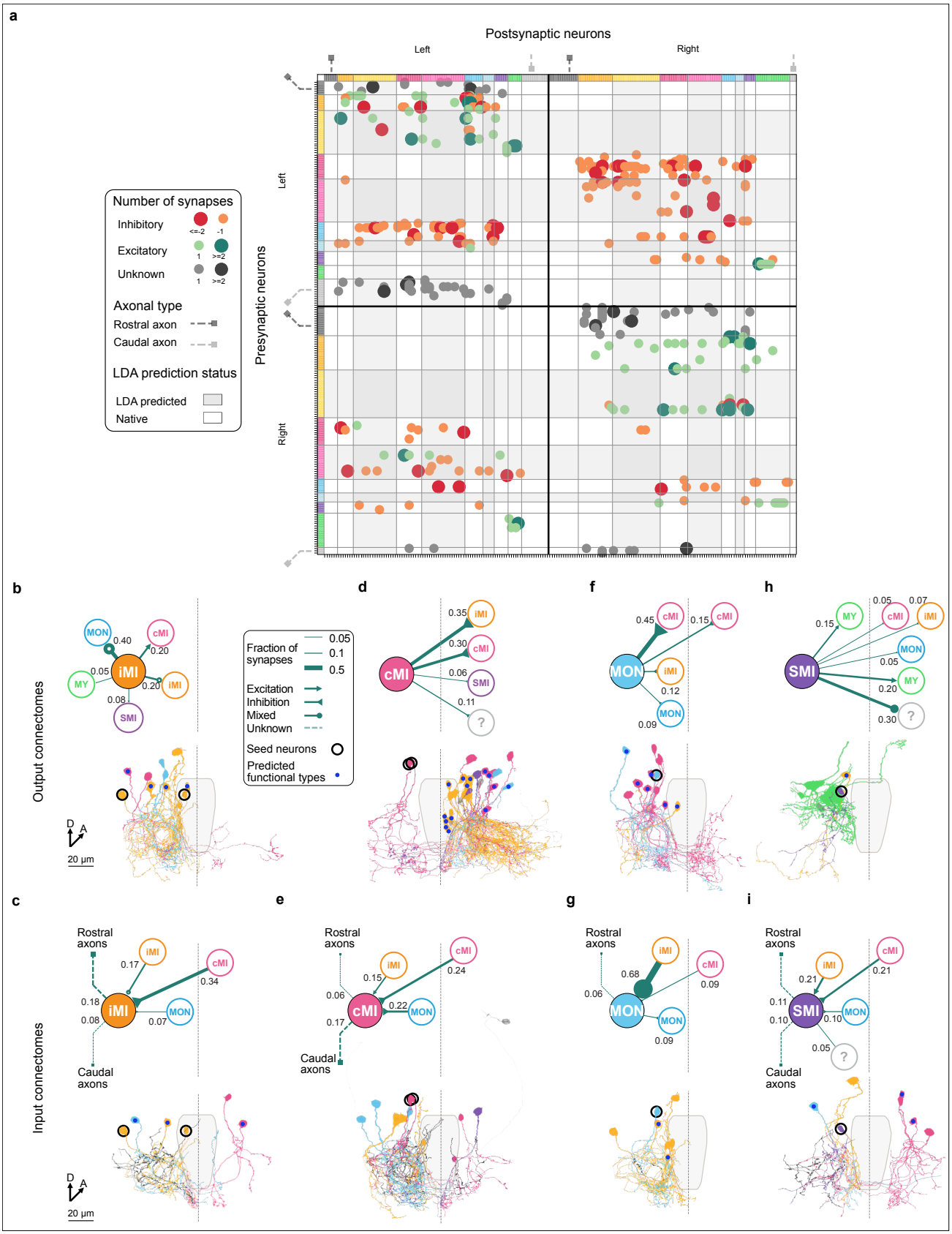

Extended Data Fig. 7 | Enhanced connectome of the zebrafish anterior hindbrain. a, Connectivity matrix with neurons and connected axons sorted according to their functional types and hemispheres (thick black bars). Rostral axons, truncated at the rostral end of the imaging volume, terminate within the volume, while caudal axons are truncated at the caudal end of the volume and also terminate within it. Axons that traverse the entire imaging volume are not shown. **b–i,** Top diagrams: simplified connectivity motifs extracted from the connectivity matrix containing predicted and native identities. Connections accounting for less than 5% of the total synapse number are not shown. Bottom diagrams: Representative example connectomes (dorsal view) for one or two seed cells related to **Fig. 2c–j.** All neuronal parts (some, axon and

dendrites) are colored identically. All neurons are registered to a reference brain (Randlett, Wee, E. a Naumann, *et al.*, 2015).

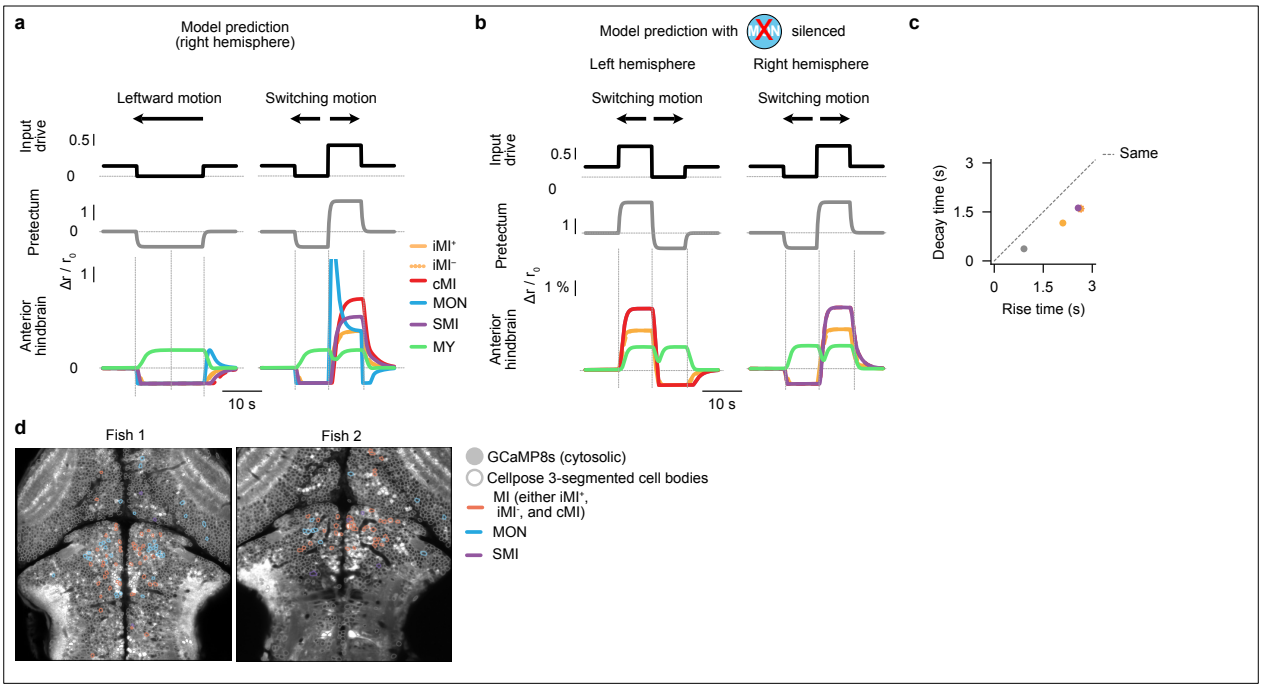

Extended Data Fig. 8 | Simulated contralateral dynamics of anterior hindbrain cell types, ablation simulations, and raw imaging stacks. a, Same as in **Fig. 4d**, but for cells on the right brain hemisphere, when the motion stimulus starts moving to the left. **b,** Switching motion stimulus, as in **Fig. 4d**, for left and right brain hemispheres, for a network model in which MON cells have been silenced (rates clamped to zero). **c**, Rise and decay times (**Methods**) for all remaining model cells for dynamics in the left hemisphere (cMI dot, red, is behind SMI dot, magenta). **d,** Raw average two-photon imaging planes of 2 example larvae, exemplifying the expression of Tg(*elavl3:GCaMP8s*) and cellpose3 segmentation results (gray contours). Segmented and functionally assigned cell types, highlighted in colored cell body contours.

Extended Data Table 1 | All extracted 68 neuron morphometrics used to generate our functional cell type classifier.

#	Name	Extraction strategy
1	number of contralateral branches	custom code
2	number of ipsilateral branches	custom code
3	**cable length**	navis
4	**bbox volume**	navis
5	**x_extent**	navis
6	**y_extent**	navis
7	z_extent	navis
8	**x average**	custom code
9	**y average**	custom code
10	z average	custom code
11	soma x	custom code
12	soma y	custom code
13	soma z	custom code
14	tortuosity	navis
15	n_leafs	navis
16	n_branches	navis
17	n_ends	navis
18	n_edges	navis
19	main_branchpoint	navis
20	n_persistence_points	navis
21	max_strahler_index	navis
22	sholl_distance_max_branches	navis
23	sholl_distance_max_branches_cable_length	navis
24	sholl_distance_max_branches_geosidic	navis
25	sholl_distance_max_branches_geosidic_cable_length	navis
26	main_path_longest_neurite	custom code
27	main_path_total_branch_length	custom code
28	first_major_branch_longest_neurite	custom code
29	first_major_branch_total_branch_length	custom code
20	first_branch_longest_neurite	custom code
31	first_branch_total_branch_length	custom code
32	cable_length_2_first_branch	navis
33	z_distance_first_2_first_branch	navis
34	biggest_branch_longest_neurite	custom code
35	biggest_branch_total_branch_length	custom code
36	longest_connected_path	custom code
37	n_nodes_ipsi_hemisphere	custom code
38	n_nodes_contra_hemisphere	custom code
39	n_nodes_ipsi_hemisphere_fraction	custom code
40	n_nodes_contra_hemisphere_fraction	custom code
41	**x_location_index**	custom code
42	**fraction_contra**	custom code
43	**y_extent_ipsi**	custom code
44	**z_extent_ipsi**	custom code
45	**max_x_ipsi**	custom code
46	**max_y_ipsi**	custom code
47	max_z_ipsi	custom code
48	min_x_ipsi	custom code
49	min_y_ipsi	custom code
50	min_z_ipsi	custom code
51	max_x_contra	custom code
52	max_y_contra	custom code
53	max_z_contra	custom code
54	min_x_contra	custom code
55	min_y_contra	custom code
56	min_z_contra	custom code
57	avg_delta_death_birth_persitence	navis
58	median_delta_death_birth_persitence	navis
59	std_delta_death_birth_persitence	navis
60	z_extent_contra	custom code
61	y_extent_contra	custom code
62	midline crossing x	custom code
63	midline crossing y	custom code
64	midline crossing z	custom code
65	crossing angle	custom code
66	crossing angle 2D	custom code
67	**morphology (ipsilateral or contralateral)**	custom code
68	neurotransmitter (exc., inh., or unknown)	custom code

The list of all 68 morphometrics we extracted from each cell to build our functional cell type classifier. We used the navis package to compute features directly from .swc files and developed custom code to further extend feature space. Through a feature ranking with reverse feature elimination algorithm (see **Methods**), we identified 7 feature to be the best predictor of function (highlighted in red).